CHAPTER 5

Synthesis, application and optimization studies of polyaniline/activated carbon/cobalt ferrite based composite material

5.1 Introduction

In the previous chapter (chapter 4), it was observed that the ternary composite PANI/AC/CuCo demonstrated the best electrochemical performance as compared to PANI and binary composite materials PANI/AC and PANI/CuCo. The ternary composite PANI/AC/CuCo was further optimized in terms of the weight ratio of the constituent components for the best electrochemical properties. In the current chapter, a comparison of the electrochemical properties of pristine polyaniline (PANI), binary polyaniline-activated carbon (PANI/AC), binary polyaniline- cobalt ferrite (PANI/CoF), and ternary polyaniline-activated carbon-cobalt ferrite (PANI/AC/CoF) has been discussed.

For the synthesis of PANI, 9.40 g of aniline monomer along with 28.5 g of ammonium persulfate and 8.61 g of p-toluene sulfonic acid was taken. For the preparation of binary and ternary composite materials, 2.30 g of activated carbon and 2.3 g of cobalt ferrite were used so that the corresponding weight ratio in the composite materials is 4:1 (PANI:AC), 4:1 (PANI/CoF) and 4:1:1 (PANI/AC/CoF), respectively. In the latter part of this chapter, optimization studies of the weight percentage of the ternary composite material have been performed. Through these comparative and optimization studies, we aim to identify the composite material composition that yields the best electrochemical performance with a focus on specific capacitance, specific energy density, specific power density and cycle life.

Part I: Electrochemical performance of pristine PANI, binary PANI/AC, binary PANI/CoF, and ternary PANI/AC/CoF composite materials.

5.2 Result and discussion

5.2.1 X-ray diffraction (XRD) patterns

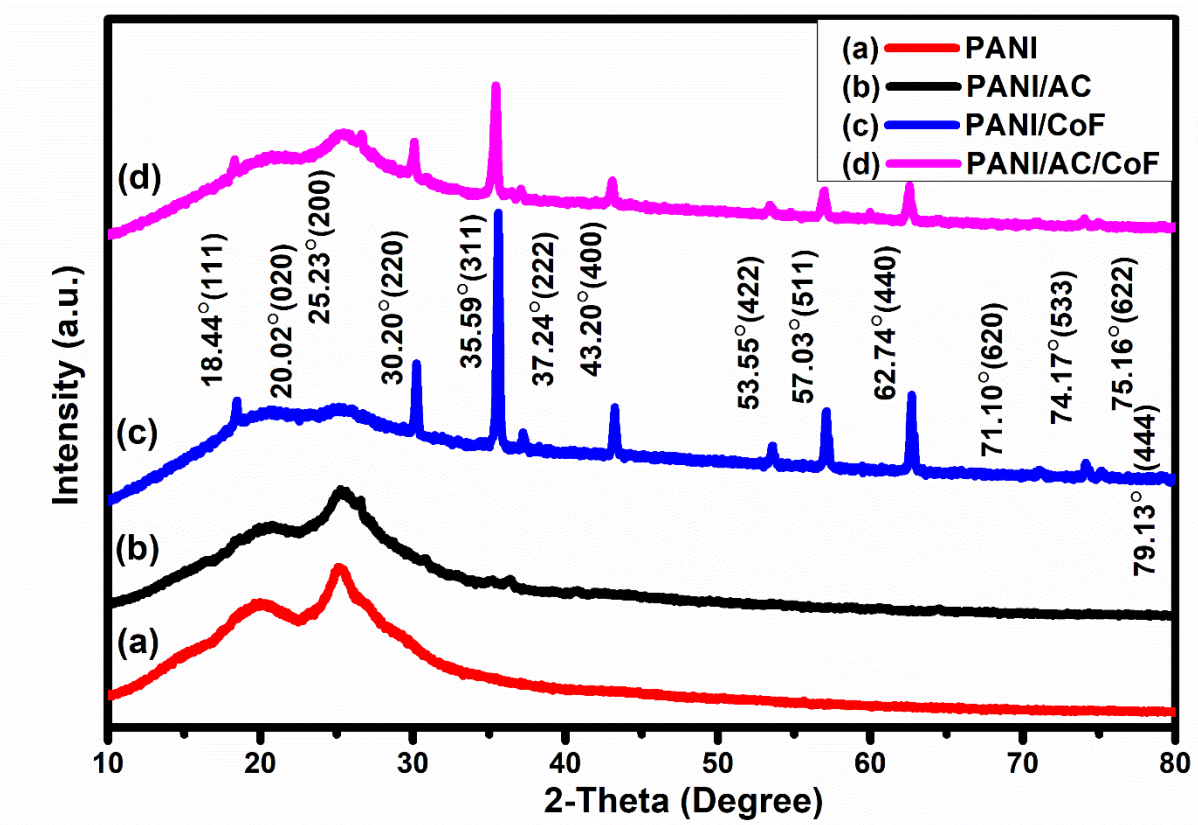

Fig 5.1: XRD patterns of pristine PANI, binary PANI/AC, binary PANI/CoF, and ternary PANI/AC/CoF

The X-ray diffraction (XRD) spectra were employed to confirm the successful synthesis of the prepared materials, as demonstrated in figure 5.1. The successful synthesis of PANI was confirmed by humps present at 20.01° (020) and 25.21° (200) [248]. The characteristic diffraction peak of AC (Fig. A1 in appendix) may have merged with the PANI peak to form a single sharp peak at 25.39° in the case of binary PANI/AC (appendix). PANI and AC are known to show π-π* stacking interactions, which enhances the electron transfer efficiency for the composite material. The peaks at 18.36° (111), 30.12° (220), 35.46° (311), 37.09° (222), 43.13° (400), 53.51° (422), 57.06° (511), 62.55° (440), 71.07 (620), 75.02° (622) and 79.11°

(444) indicate the successful synthesis of cobalt ferrite particles (JCPDS 22-1086) (Fig. A1 (C) in appendix). The crystalline size obtained from Bragg's formula (eq. 3.5) was found to be 51.38 nm. The peaks present at 18.44° (111), 30.20° (220), 35.59° (311), 37.24° (222), 43.20° (400), 53.55° (422), 57.03° (511), 62.74° (440), 71.10° (620) 75.16° (622) and 79.13° (444) confirmed the presence of CoF particles in PANI to form PANI/CoF. Further, all the expected spikes of PANI, PANI/AC, and PANI/CoF could be seen in the ternary composite PANI/AC/CoF material to mark the successful synthesis of the ternary composite material.

5.2.2 FTIR

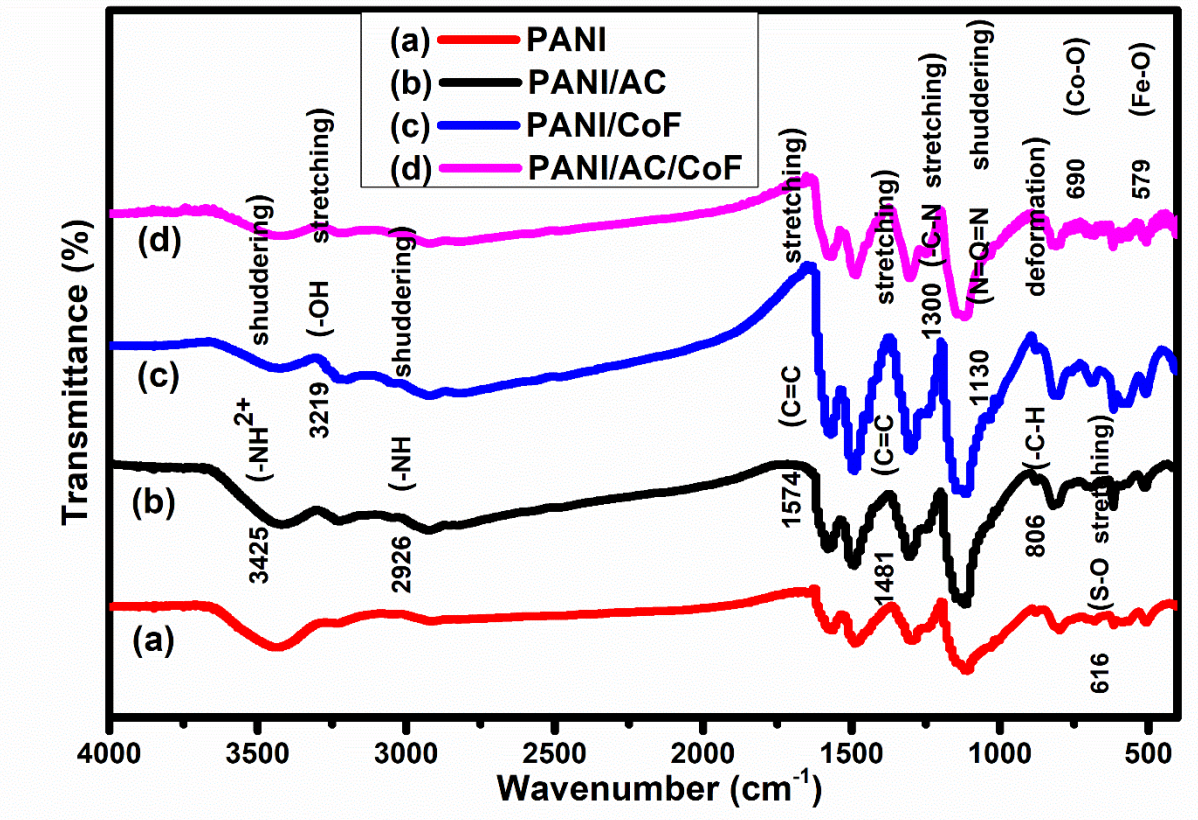

Fig 5.2: FTIR spectra of pristine PANI, binary PANI/AC, binary PANI/CoF, and ternary PANI/AC/CoF

The FTIR spectra for the prepared samples PANI, PANI/AC, PANI/CoF, and PANI/AC/CoF were recorded and have been presented in figure 5.2. For PANI, the band at 3428 cm^{-1} was

associated with -$NH^{2+,}$ and -OH bending was indicated by the band at 3222 cm^{-1}[228,229]. The band at 2926 cm^{-1} was present due to -NH stretching vibrations [228]. The quinoid band impressions at 1574 were less intense than 1481 cm^{-1} benzoid band C=C vibrational stretching, which indicates the presence of benzoid form in higher amounts. This higher intensity of benzoid form was also observed in composite materials. The C-N stretching vibrations were indicated by the band at 1300 cm^{-1} due to the presence of protonated PANI. The p-substituted group with N=Q=N stretching vibrations in the case of PANI was present at 1130 cm^{-1}. The peak at 806 cm^{-1} was attributed to -CH deformation indicating the presence of PTSA in PANI [231]. The -SO_3 asymmetric vibration of PANI was indicated by the peak at 616 cm^{-1}. For AC, a strong stretching band observed at 3430 cm^{-1} could be attributed to the presence of O-H due to moisture content. The characteristic AC band at 1070 cm^{-1} was present due to C-O stretching vibrations (Fig. A2 (A) in appendix). The presence of C-O is responsible for π-π* interactions between AC particles and aniline monomer, as discussed in the previous chapter. In the case of binary PANI/CoF, bands at 579 and 690 cm^{-1} indicated the presence of Fe-O and Co-O. Also, the overall intensity of absorption spectra was higher in PANI/CoF than in PANI/AC/CoF, which may be due to the dispersion of CoF in AC and then swaddling by PANI. The strong characteristic peak of PANI is shifted to a slightly higher value in the composite materials, which may be due to the presence of protonated PANI. All the corresponding bands could be distinguished with slight shifting in the case of ternary composite PANI/AC/CoF.

5.2.3 Morphological Analysis

The FESEM images for pristine PANI, binary PANI/AC, binary PANI/CoF, and ternary PANI/AC/CoF have been presented in figure. 5.3. PANI manifests mostly rod-like structures which are interconnected. In the case of binary PANI/AC, these rod-like structures are visible, but there is some unevenness due to the presence of AC. This uneven type of morphology gets more dominant and covers the surface in the case of PANI/CoF, which may be due to the

conversion of the micelle-like PTSA-aniline complex into nanorods. In the case of ternary PANI/AC/CoF hybrid ternary composite, compact and uneven structures are mostly present due to activated carbon and cobalt ferrite particles. This type of structural aggregation may be responsible for the enhanced solid-electrolyte interfacial area and consequently supports the rapid transportation of electrolyte ions during the charging-discharging process [249]. The FESEM micrographs of AC and CoF have been presented in fig. A3 (in appendix)

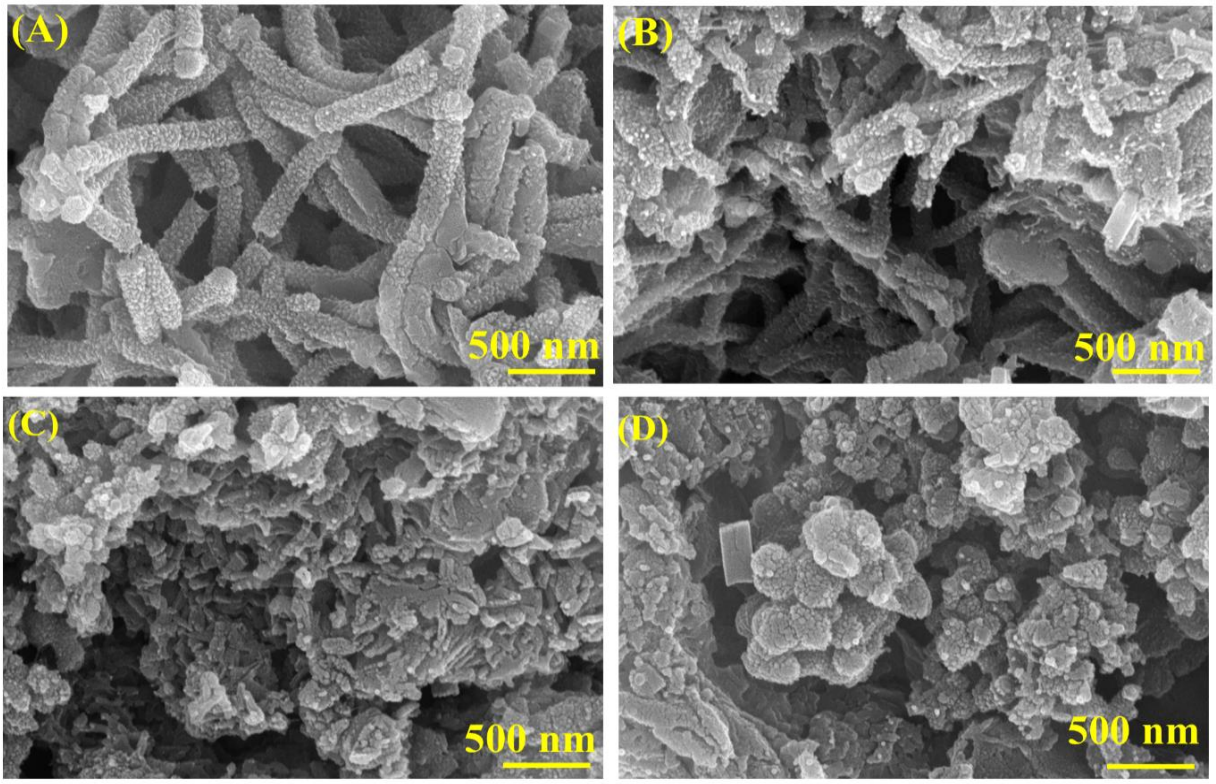

Fig 5.3: FESEM micrographs of (A) PANI, (B) PANI/AC, (C) PANI/CoF, and (D) PANI/AC/CoF

5.2.4 EDX and elemental mapping

The details of the elemental analysis of the prepared materials PANI, PANI/AC, PANI/CoF, and PANI/AC/CoF have been presented in figure 5.4, showing the presence of all the expected elements. The elemental analysis results indicate that C % has increased in the case of PANI/AC as compared to PANI, which may be due to the incorporation of AC into PANI. The

C % was reduced in the composite materials PANI/CoF and PANI/AC/CoF due to the incorporation of other elements. The N % decreased significantly in the case of PANI/AC due to the addition of C and O in the form of AC. The low composition of S was attributed to extensive washing of the sample to remove the excessive monomer and oxidant. There was no significant change in the composition of O. In the case of binary PANI/CoF and ternary PANI/AC/CoF, the atomic ratio of Co and Fe is approximately 0.5, which is relatable from the formula $CoFe_2O_4$. The presence of K was also observed which is due to the activation of AC with KOH.

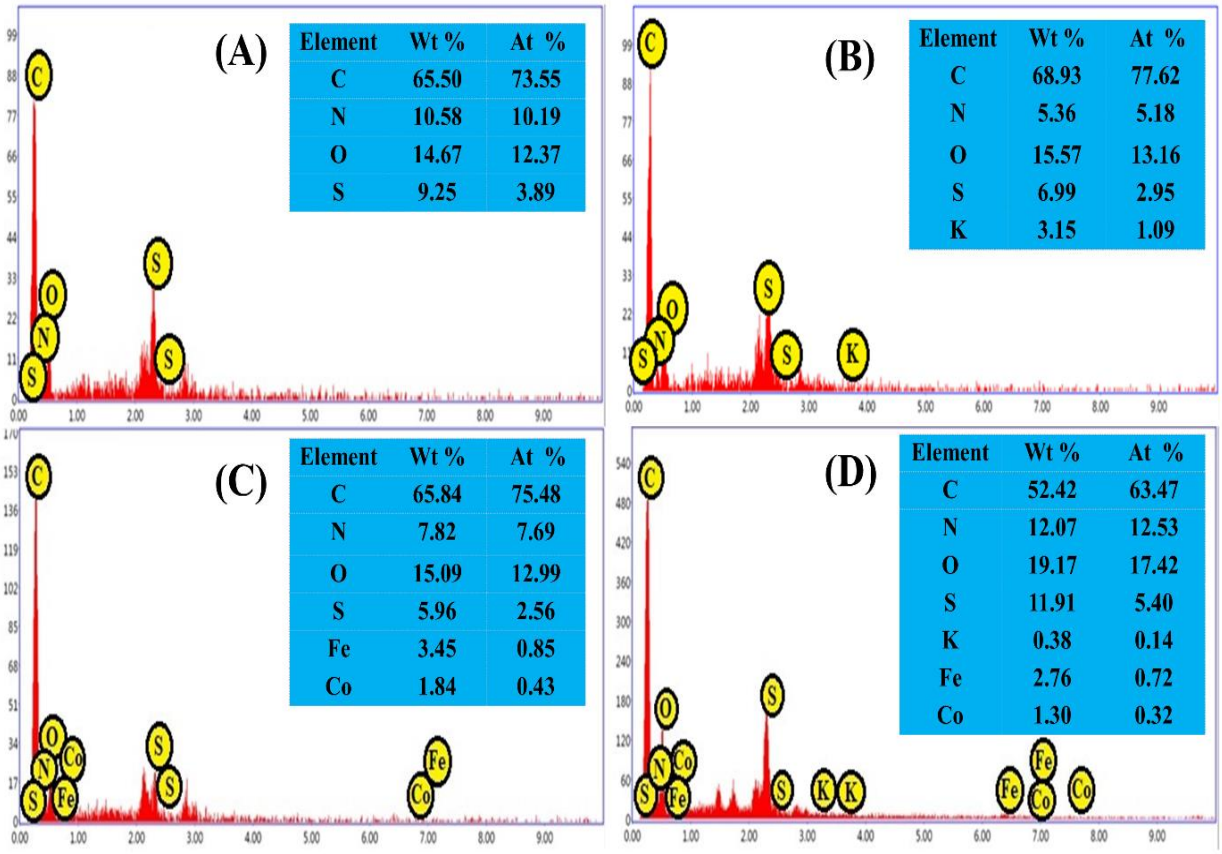

Fig 5.4: EDX analysis of (A) PANI, (B) PANI/AC, (C) PANI/CoF, and (D) PANI/AC/CoF

The elemental mapping (combined and individual) of the ternary composite material PANI/AC/CoF has been demonstrated in figure 5.4. A uniform mapping pattern could be observed in figure 5.5 (a). Also, the mapping patterns of C, N, O, and S demonstrate their

higher concentration as compared to that of K, Co, and Fe in the ternary composite PANI/AC/CoF in figure 5.5 (b) to (h).

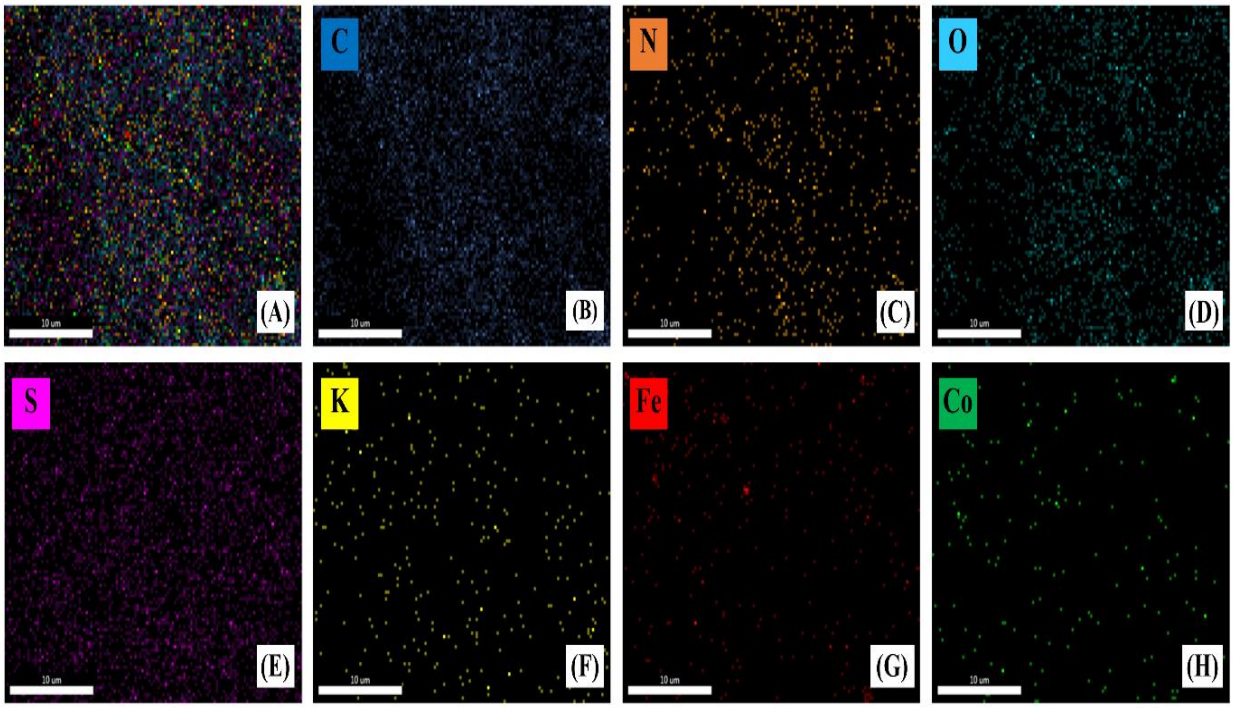

Fig 5.5: Elemental mapping of ternary composite material PANI/AC/CoF.

5.2.5 X-ray photoelectron spectroscopy (XPS)

The composition of the synthesized nanomaterials was confirmed using X-ray photoelectron spectroscopy. Figure 5.6 (A) shows the survey scan of pristine PANI, PANI/AC, PANI/CoF, and ternary PANI/AC/CoF demonstrating the presence of C, N, O, and S in all the samples. The presence of Co and Fe could also be observed in the case of PANI/CoF and ternary PANI/AC/CoF. Further, figure. 5.6 (B) to (F) manifest the high-resolution spectra for ternary PANI/AC/CoF. The high-resolution fitted spectrum of PANI/AC (Fig. A4 in appendix) demonstrated four different peaks at 284.51 eV, 285.51 eV, 286.92 eV, and 290.71, respectively. These peaks can be attributed to (C-C) & (C=C), (C-O), (C=O) groups and π-π* "shake-up" satellite band due to the presence of AC, respectively.

In the case of ternary PANI/AC/CoF, C1s high-resolution spectra (Figure. 5.6 (B)) revealed five distinct peaks. The (C-C) & (C=C) were assigned for binding energy 284.39 eV. The (C-N) group was attributed to 284.76 eV. The (C-O) in alkoxy/epoxy was assigned to 285.77 eV, (C=O) in carboxylic groups was ascribed to 288.77 eV, and the (O-C=O) group with 290.96 eV, respectively. The N1s spectra (Figure. 5.6 (C)) showed two peaks at 399.71 and 401.36 eV that were attributed to N cationic radical and benzoid amine (-NH-). The presence of PANI in the form of conducting form of PANI was confirmed by these two peaks [239]. The O1s spectra (Figure. 5.6 (D)) resolved into three distinctive peaks. The peak at 531.86 eV was present due to (C=O) from aromatic carbon, the peak at binding energy 533.48 eV was attributed to a carbon-oxygen single-bond group (C-O), and that at 534.4 eV was due to (C-OH) group (carbon-hydroxyl) [240,241].

Also, the two sharp peaks at 780.59 and 796.02 eV were present due to Co $2p_{3/2}$ and Co $2p_{1/2}$ with their respective satellite peaks at 785.6 and 802.8 eV, as shown in figure. 5.6 (E) [240]. These peaks confirm the presence of Co in the ternary composite. The Fe spectra (Figure. 5.6 (F)) in ternary nanocomposite PANI/AC/CoF deconvoluted into two strong and one satellite peak. A sharp peak indicated the presence of Fe 2p3/2 binding energy 711.52 eV, and its satellite peak at 715.49 eV [250]. Further, a relatively wider peak at 725.15 eV corresponds to the presence of Fe $2p_{1/2}$ [242,243].

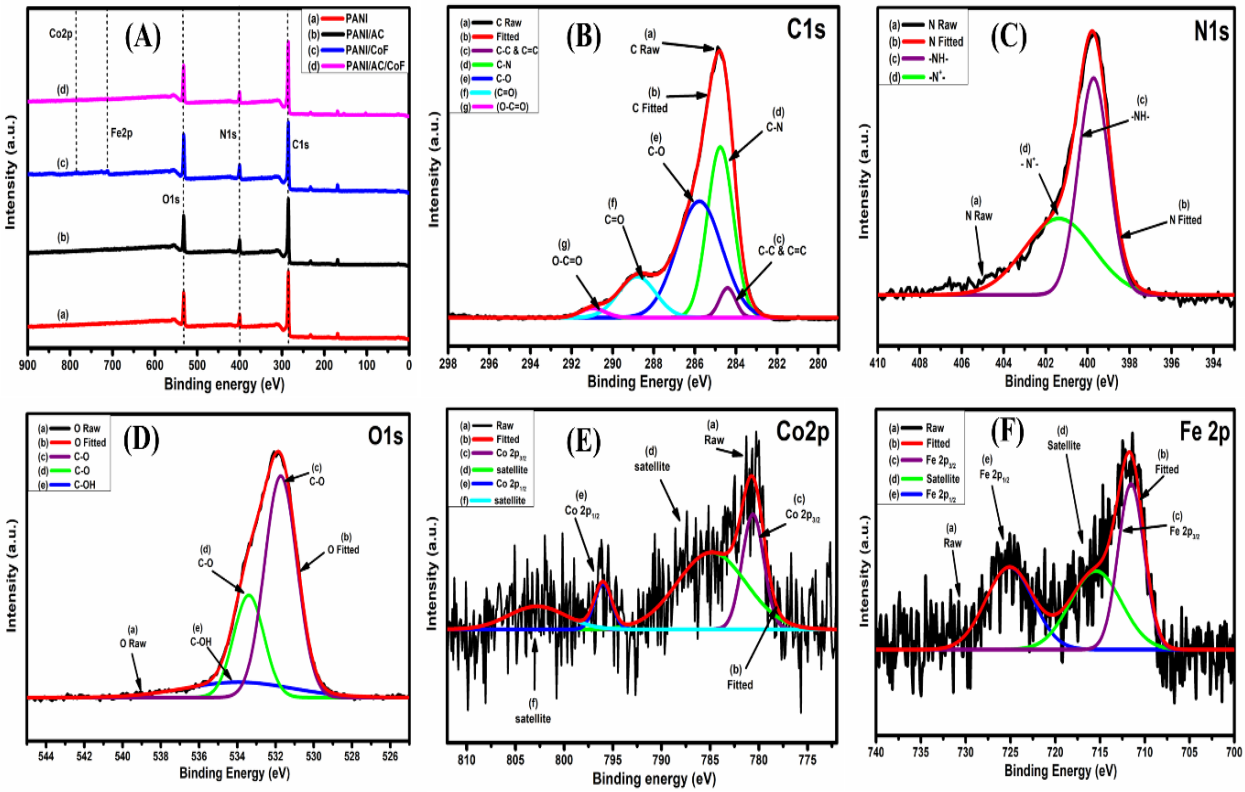

Fig 5.6: (A) XPS survey scan of PANI, PANI/AC, PANI/CoF, PANI/AC/CoF, (B) to (F) high-resolution spectra for C1s, N1s, O1s, Co2p and Fe2p, respectively.

5.2.6 Transmission electron microscopy

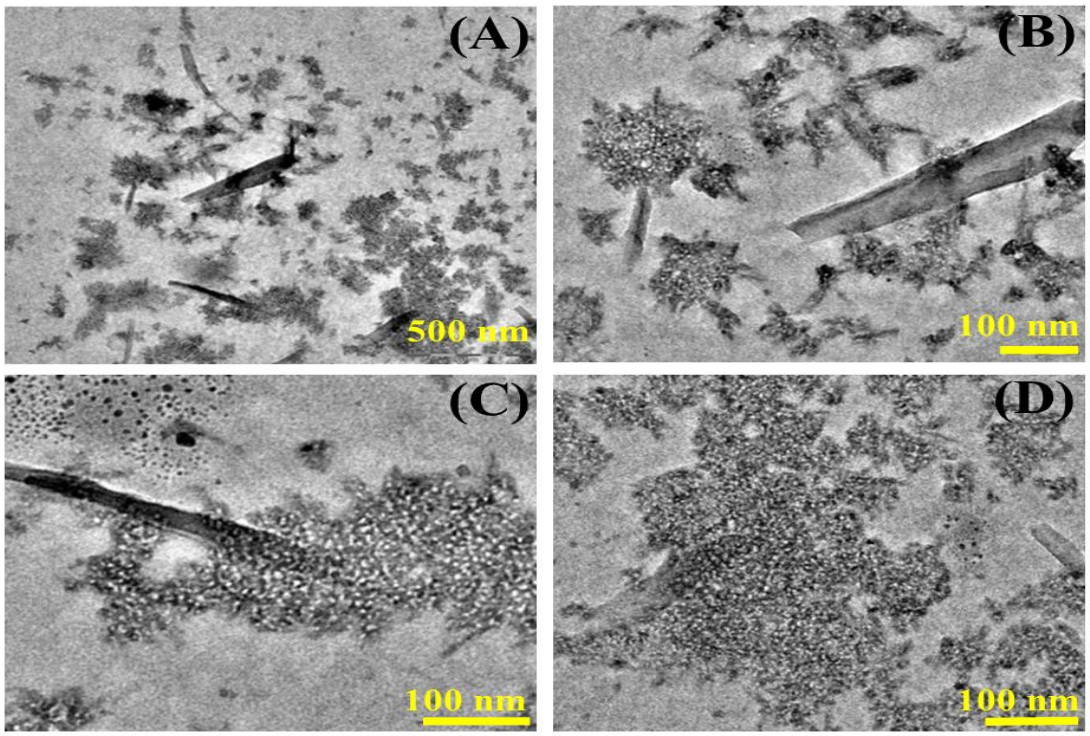

Fig 5.7: (A) to (D) TEM micrographs of ternary composite material PANI/AC/CoF

Figure 5.7 (A) to (D) demonstrates TEM micrographs of ternary nanocomposite PANI/AC/CoF. The presence of PANI nanorods is visible, which is relatively larger as compared to AC and CoF particles. It is also evident that the smaller CoF particles were intercalated into porous AC support, which confirmed the successful implementation of the morphology strategy regulation, as discussed in chapter 2.

5.3 Electrochemical Characterizations

The 3E CV tests for prepared samples were conducted at 1 mVs^{-1}, as shown in figure. 5.8 (A). With oxidation peaks at 0.27, 0.59, and 0.71 V and corresponding reduction peaks at 0.04, 0.40, and 0.63 V, PANI showed three distinct redox (reduction-oxidation) peaks. The transition from the leucoemeraldine to the emeraldine state was attributed to the peak at 0.27 V. The peak at 0.59 V was caused by hydroquinone/benzoquinone degradation. The peak at 0.71 V was associated with a transition from the emeraldine state to the pernigraniline state [251,252]. Different redox transitions of PANI have been presented in fig. A5 in appendix. The specific capacitance exhibited by pristine PANI was 394.6 Fg^{-1}. Binary PANI/AC, PANI/CoF, and ternary PANI/AC/CoF did not exhibit the PANI peak at 0.59 V, which may have been caused by the inclusion of AC and $CoFe_2O_4$ particles. The binary composite PANI/AC exhibited redox peaks at 0.21/0.70 for forward and 0.51/0.09 for backward scans. The CV of PANI/AC exhibited a combination of EDLC and pseudocapacitance with a larger voltammetric area than pure PANI, indicating its better specific capacitance at 530.3 Fg^{-1}.

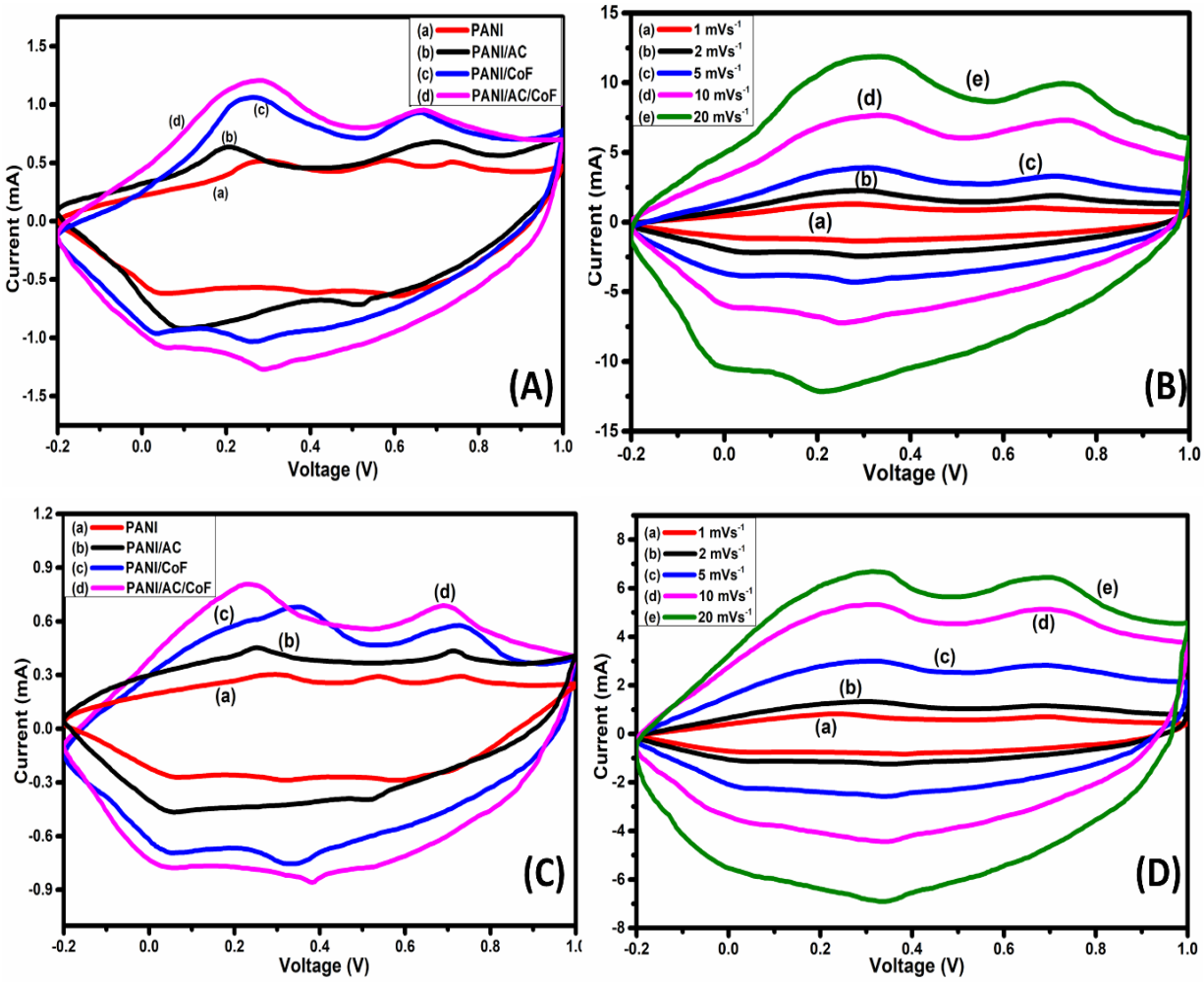

Fig 5.8: (A) 3E CV of prepared materials, (B) 3E CV of ternary PANI/AC/CoF at varying scan rates, (C) 2E CV of prepared materials, (D) 2E CV of ternary PANI/AC/CoF at varying scan rates

Furthermore, in the case of PANI/CoF, the transitions due to Co^{2+}/ Co^{3+} and Co^{3+}/ Co^{4+} correspond to the oxidation peaks at 0.26 V and 0.66 V, respectively. The third redox peak due to Fe^{6+}/ Fe^{3+} switchover is not visible due to its merger with the PANI peak at 0.71V in the same region. A redox reaction mechanism of $CoFe_2O_4$ has been presented in appendix (eq. B). The binary PANI/CoF demonstrated a specific capacitance of 571.7 Fg^{-1}. The voltammetric area under curves is highest for PANI/AC/CoF-based ternary material with higher peak current values with 640.8 Fg^{-1} of specific capacitance. The value of the specific capacitance of the ternary composite PANI/AC/CoF is much higher than that reported in previous investigations

[253–258]. The interconnected structures in the case of ternary PANI/AC/CoF visible in the high-resolution microscopic images may be responsible for the highest voltammetric area. The porous structure of AC creates channels for ion transport, thus, the PANI and CoF deep inside the active material can easily participate in the redox reactions. Multiple scan rates of 2, 5, 10, and 20 mVs^{-1} were used to study the behavior of ternary nanocomposite PANI/AC/CoF (Figure. 5.8 (B)), which manifested specific capacitance of 564.3, 487.6, 412.8, and 309.8 Fg^{-1}, respectively. The peak current responses rise with the increase in scan rate, implying rapid charge propagation. With increasing scan rates, the area under the CV curves rises, showing the ternary composite material is highly capacitive. Also, forward scan peaks were shifted to a more positive direction, whereas reverse scan moved to a more negative direction, indicating the presence of strong capacitive and faradaic currents. This shifting of redox peak may be attributed to strong electric polarization and possible kinetic irreversibility of electrolyte ions at the electrode-electrolyte interface.

For 2E symmetric configurations, the CV was performed at $1mVs^{-1,}$ as demonstrated (Figure. 5.8 (C)). Again, the ternary nanocomposite PANI/AC/CoF exhibited the highest voltammetric area. The combination of EDLC and the pseudocapacitive nature of the materials may be responsible for high voltametric area. Further, with the rise in scan rates, the voltammetric area of CV curves increases as shown in figure. 5.8 (D), which may be attributed to the rising capacitive current increase in voltammetric scan rates. The electrolyte ions, however, don't get sufficient time to travel to the active sites as scan speeds increase, which causes a decrease in specific capacitance. Therefore, it cannot reciprocate with corresponding reversible redox reactions compared to that at lower scan rates.

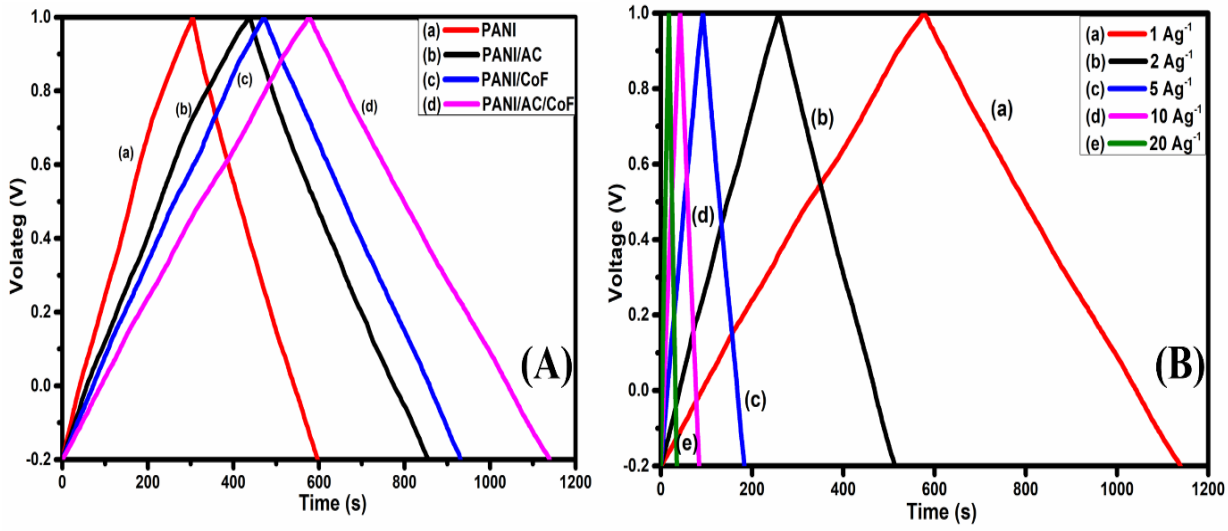

Fig 5.9: GCD characteristics of (A) PANI, PANI/AC, PANI/CoF, and PANI/AC/CoF at 1 A/g, (B) ternary PANI/AC/CoF at varying current density

The charging and discharging behavior of the fabricated electrodes has been presented in figure. 5.9 (A). All the materials depicted symmetric triangular nature with few deviations or plateaus. The contribution of redox transitions, EDLC, and pseudocapacitive behavior may cause these deviations. A variation of current densities from 2 to 20 Ag^{-1} for PANI/AC/CoF was also performed, as shown in figure. 5.9 (B). The charge-discharge plots of PANI/AC/CoF retained their symmetrical triangular nature intact with rising values of current density up to 20 Ag^{-1}. Also, both the charging and discharging times diminished due to ions' inaccessibility to certain packets at higher currents. These inactive sites pose an ion diffusion barrier for the electrolyte ions. These highly linear and symmetric GCD profiles at all the different current densities imply the electrodes' excellent reversibility and good rate capability.

The Ragone plots for the prepared samples have been shown in figure. 5.10 (A), ternary PANI/AC/CoF exhibited the highest specific energy density as compared to PANI/AC, PANI/CoF, and PANI. Table 5.1 demonstrates the values of specific capacitance, specific energy density, and power density for different synthesized materials. The ternary composite exhibited more charge storage capacity than other materials, as indicated by the specific power

density. Additionally, it was observed that the specific energy diminished with rising specific power with the rise in current densities. Figure 5.10 (B) demonstrates the change of 3-E specific capacitance with a change in voltammetric scan rates which decreases with a rise in the value of the scan rate.

Table 5.1: The values of specific capacitance (C_{SP}), specific energy (E_{SP}), and specific power density (P_{SP}) for different synthesized materials

Material	**Scan Rate (mV/s)**	**C_{SP} (CV 3-E)**	**Current Density (A/g)**	**Esp (Wh/kg)**	**Psp (W/kg)**
PANI	1	394.6	1	25.4	300.2
PANI/AC	1	530.3	1	34.0	300.3
PANI/CoF	1	571.7	1	38.1	298.1
PANI/AC/CoF	1	640.8	1	46.9	301.9
PANI/AC/CoF	2	564.3	2	42.0	598.9
PANI/AC/CoF	5	487.6	5	37.4	1499.8
PANI/AC/CoF	10	412.8	10	33.5	2997.7
PANI/AC/CoF	20	309.8	20	28.2	6002.3

The charge transfer capacity can be broadly measured using coulombic efficiency. According to GCD plots, it is the ratio between the charging and discharging times. The variation of coulombic efficiency vs. current density for ternary PANI/AC/CoF is depicted in figure. 5.10 (C). As current density rises, the coulombic efficiency falls, probably because the material is more irreversible at these current densities. At 20 A/g, the ternary composite had astounding coulombic efficiency of 92.8%.

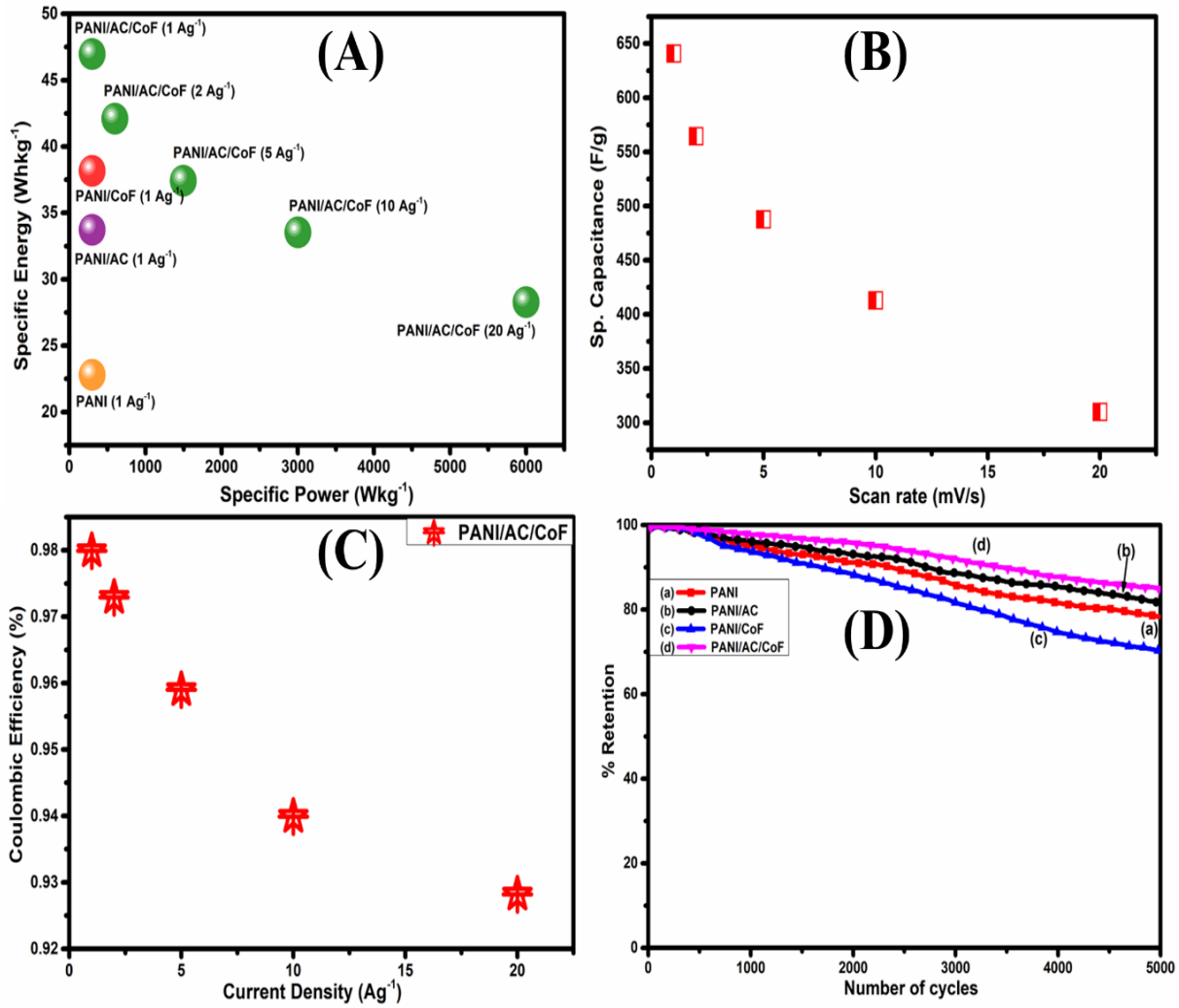

Fig 5.10. (A) Ragone plot for the prepared samples, (B) Comparison of 2E and 3E specific capacitance values at different values of voltammetric scan rates, (c) current density vs. coulombic efficiency, (D) Capacitance retention curve

In order to examine the capacitance retention of the prepared electrodes, the cyclic stability tests for the symmetric device were also conducted for 5000 cycles at 100 mV/s, as provided in figure. 5.10 (D). PANI/AC/CoF, the ternary composite, exhibited a capacitance retention of 84.56 %, which is much higher than that of PANI/CoF, PANI/AC, and pure PANI samples. The binary composite PANI/ CoF exhibited abrupt fluctuations, restricting their cycling capability; therefore, incorporating porous AC strengthens its overall structure and reduces uneven changes while improving cycle stability.

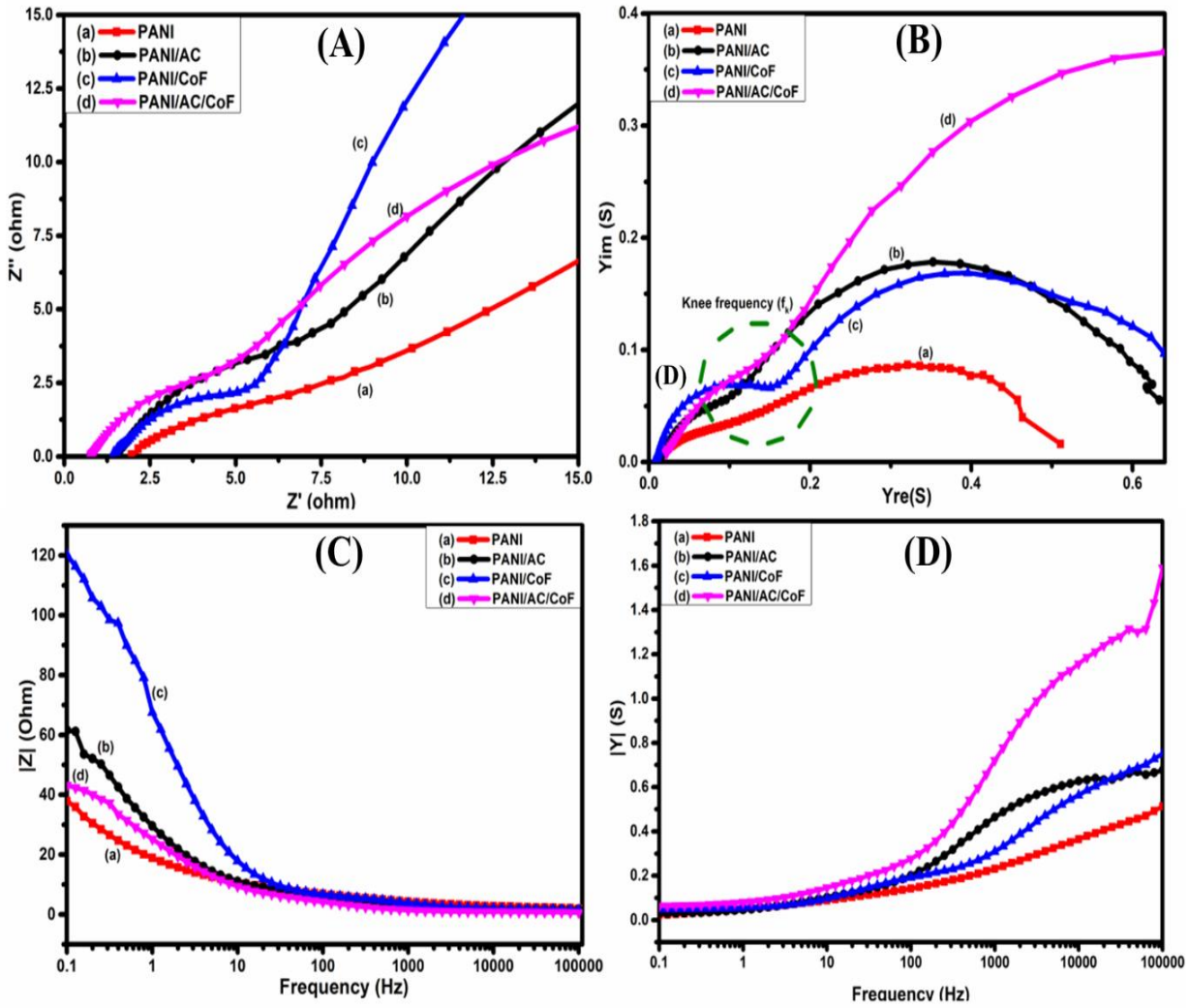

Fig 5.11: (A) Electrochemical impedance spectra (EIS) in the complex plane (B) Admittance plots in the complex plane. (C) normalized impedance |Z| vs. frequency, (D) normalized admittance vs. frequency

In order to determine equivalent series resistance (ESR), Warburg resistance (Rw), and charge transfer resistance (Rct), EIS studies were conducted for the prepared samples. ESR represents the sum of all the components, such as electrode-electrolyte contact resistance, material resistance, and electrolyte solution resistance. The abscissa intercept in the high-frequency region reflects equivalent series resistance (ESR), and the semicircle represents charge transfer resistance (Rct). PANI/AC/CoF-based electrode demonstrated a low ESR of 1.01 Ω and Rct of 6.2 Ω. PANI/CoF, PANI/AC, and pure PANI showed ESR / Rct at 1.49 / 6.52 Ω, 1.6/ 7.3, and 1.5/ 7.6 Ω, respectively, as shown in figure. 5.11 (A). These lower resistance values could

cause the ternary composite PANI/AC/CoF's high capacitance retention characteristic and linear charge-discharge curve. The results confirm that substrate, current collector, and electrolyte offer low resistances and fast ion diffusion with rapid charge transfer with processes. The results illustrate that the electrolyte, substrate, and current collector provide low resistances, quick ion diffusion, and quick charge transfer processes.

Frequency response investigations were conducted to assess the behavior of normalized admittance |Y|, impedance |Z|, capacitance |C|, and phase of Z as a function of frequency. Figure. 5.11 (B) demonstrates the plot between real and imaginary components of total admittance |Y| for the prepared samples. Additionally, the relaxation time constant (tr), the minimum time required to extract all supercapacitor energy with at least 50 % efficiency, is inversely related to knee frequency (fk).

The supercapacitor transitions between resistive and capacitive behavior at a frequency known as knee frequency. For ternary PANI/AC/CoF, PANI/CoF, PANI/AC, and PANI, the values of f_k obtained were 0.025, 0.006, 0.05, and 0.10 Hz, with corresponding response times ($t_{r)}$ at 39.81, 158.48, 19.95 and 10 Hz. All the systems except binary PANI/CoF exhibit quick response times due to redox-active materials (PANI and CoF), creating a sluggish system (taking more time to respond due to redox transitions and volumetric deformations).

Figure 5.11 (C) manifests normalized impedance |Z| vs. frequency for pure PANI, PANI/AC, PANI/CoF, and PANI/AC/CoF. The general trend is that |Z| decreases with increased frequency for all the materials as impedance is reciprocal of admittance. The pristine PANI exhibited the highest total impedance value |Z|, whereas the ternary composite PANI/AC/CoF exhibited the lowest value. The other two binary composites viz. PANI/AC and PANI/CoF showed intermediate values of total impedance |Z|. Figure. 5.11 (D) represents the plot of normalized admittance |Y| with frequency for PANI, PANI/AC, PANI/CoF, and

PANI/AC/CoF. For all of the prepared samples, it was observed that |Y| increases as the frequency increases. Further, it was noted that pure PANI showed the least admittance, and ternary composite PANI/AC/CoF demonstrated the max total admittance throughout. This high admittance may be attributed to the faster movement of ions at high frequency coupled with better conductivity than other materials.

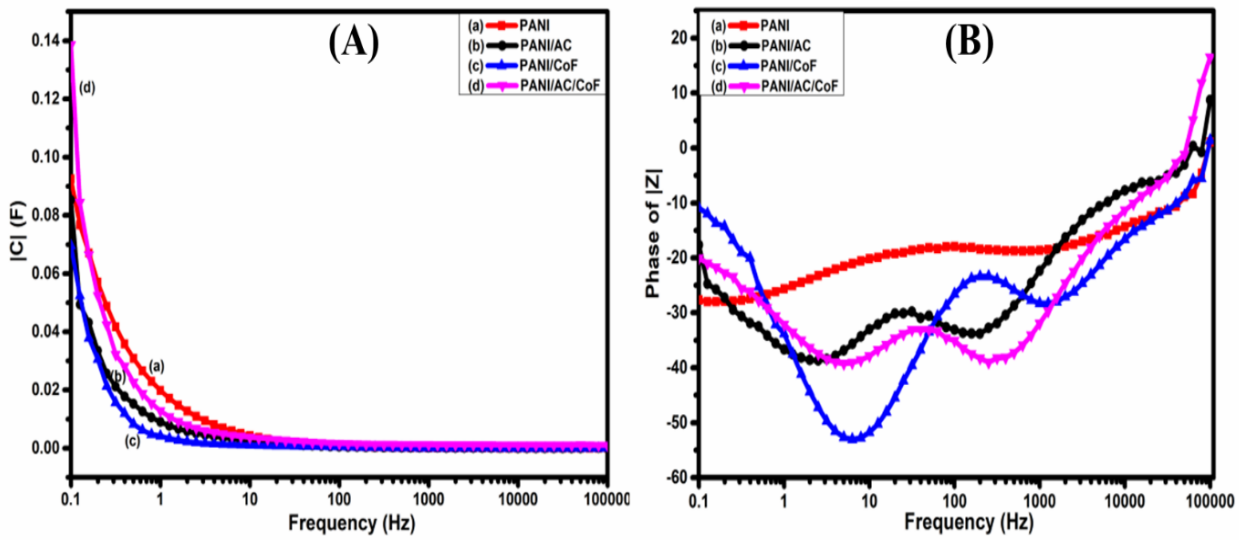

Fig. 5.12: (A) normalized capacitance |C| vs. freq, and (B) phase of |Z| (ϕ) vs. frequency

Figure. 5.12 (A) indicates the plot of normalized capacitance |C| vs. frequency. The total capacitance for all the materials declines with rising frequency, with PANI/AC/CoF exhibiting the best and PANI with the least capacitance. These results further corroborated the nature of the prepared samples under various frequency levels and were obviously in good agreement with the EIS plot's conclusion. The supercapacitors generally are resistive at high frequencies and capacitive at low frequencies [259]. The plot of phase of Z (ϕ) vs. frequency was also studied for the prepared samples, as presented in figure. 5.12 (B). For all the prepared samples, the phase of Z remains negative for a greater part of the frequency band, exhibiting the supercapacitive nature of electrodes. The phase angle is lagging at around 28° at low frequency for pristine PANI, representing its pseudocapacitive behaviour. For binary PANI/AC, due to the presence of AC, some EDLC behaviour was introduced, as evidenced by the rise in phase

angle. The binary composite PANI/CoF in the low-frequency zone showed a steep rise in phase angle to 53°, which could be due to the CoF nanoparticles agglomerating over PANI nanorods, thereby preventing the necessary redox transitions from taking place (inducing a more EDLC behavior). For ternary composite PANI/AC/CoF, by acting as a substrate for PANI and CoF, the inclusion of AC would have provided adequate skeleton or support for required redox changes to occur, thereby reducing fluctuations in phase angle as compared to binary PANI/CoF.

5.4 Conclusion

A novel ternary hybrid composite material polyaniline-activated carbon-cobalt ferrite (PANI/AC/CoF) was synthesized and characterized with the help of XRD, FTIR, FESEM, EDX, TEM, and XPS. The inherently EDLC behavior of activated carbon and the pseudocapacitive behavior of polyaniline and cobalt ferrite were responsible for the excellent electrochemical activity of the ternary composite PANI/AC/CoF. Therefore, the composite has been synthesized to take advantage of the individual components. The specific capacitance values of the ternary composite PANI/AC/CoF at 1 mVs^{-1} was 640.8 Fg^{-1}. The symmetric device based on PANI/AC/CoF demonstrated a high specific energy-density of 46.9 Wh/kg and a maximum specific power density of 6002.3 W/kg. The ternary composite PANI/AC/CoF resulted in 84.56 % of capacitance retention after 5000 cycles. This robust stability may be due to activated carbon, which maintains the inherency of polyaniline and cobalt ferrite. EDLC behavior of activated carbon and the presence of redox-active sites in polyaniline and copper cobaltite (pseudocapacitance) are responsible for the outstanding electrochemical property of the ternary composite PANI/AC/CoF. The lowest charge transfer resistance is shown in the case of ternary composite PANI/AC/CoF, which is also the system with the highest cycle life. The ternary composite's beneficial outcomes make it a good contender for supercapacitor applications.

Part II: Optimization of polyaniline-based ternary composite material PANI/AC/CoF

In this work, ternary composite material PANI/AC/CoF was optimized by varying the weight percentage of AC and CoF and taking a fixed weight percentage of PANI using the response surface methodology for supercapacitor applications.

5.5 Central Composite design

The electrochemical property of the prepared ternary composite material electrode is greatly influenced by the amount of AC and CoF used. It is essential to understand how their weight percent parameter affects the electrochemical behavior in order to improve the specific capacitance value. Hence, optimization of weight percentage of AC and CoF is important. Response Surface Methodology (RSM) is amongst the most effective and extensively used techniques for optimization. The central composite design method of RSM was utilized to optimize the weight percentage of AC (A) and weight percentage of CoF (B) in ternary composite with fixed weight percentage of PANI for electrochemical supercapacitor performance. This method offers a simple technique to assess the interactions between various variables and only calls for a limited number of experiments to optimize the response variable. Table 5.2 displays the experimental factor levels that were employed for optimization. The variables and their levels were chosen after a preliminary analysis, and the outcomes of basic experiments with 8 non-center points and 5 center points can be evaluated from the below equation.

$$N = 2^n + 2n + n_c = 2^2 + 2*2 + 5 = 13 \quad (1)$$

Where N = Total number of experiments to be performed, n = Number of independent variables, n_c = Number of centered points.

Table 5.2: Level of activated carbon (AC) and cobalt ferrite (CoF) for central composite design.

Variable	Name	Unit	Low value	High value
A (Numeric)	AC	weight percentage	1	5
B (Numeric)	CoF	weight percentage	1	5

5.6 Result and discussion

5.6.1 Optimization of ternary composite material based on RSM

13 groups of RSM experiments were produced after the experimental conditions for two influencing factors using design-expert software. Using a three-electrode configuration, the electrochemical performance of ternary PANI/AC/CoF based electrode materials was studied. The specific capacitance determined from the CV curve at the scan rate of 1 mV/s incorporated the experimental results. Table 5.3 displays the final experimental results. Regression analysis used to fit the experimental data yields the second-order polynomial equation mode shown below.

$$C\ (F/g) = +564.83 - 125.32\ A - 45.92\ B + 6.35\ AB - 15.07\ A^2 - 76.67\ B^2 \quad (2)$$

Table 5.3: The experimental data and response values obtained by central composite design.

Sample	Polyaniline (PANI) (Fixed weight percent)	Activated Carbon (AC) (Weight percent)	Cobalt ferrite (CoF) (Weight percent)	Specific Capacitance (F/g)
1	4	1	5	535.2
2	4	3	1	547.0

3	4	1	3	695.9
4	4	1	1	640.8
5	4	5	1	384.3
6	4	3	5	457.3
7	4	3	3	553.8
8	4	3	3	556.9
9	4	3	3	557.2
10	4	3	3	562.6
11	4	3	3	565.7
12	4	5	5	304.1
13	4	5	3	431.6

Analysis of variance (ANOVA) was used to determine the significance of the fitted equation, as shown in Table 5.4. The F-test resulted in a high F-value of 132.41, which suggested that the model had adequate significance ($P < 0.0001$) based on the findings of the ANOVA. The probability of getting this "model F-value" incorrectly was less than 0.01%. Typically, the P-value was employed to evaluate the importance of model terms. The related model term was more significant, as evidenced by the lower P-value. A, B, A^2, and B^2 are significant model terms in this scenario. In other terms, the precise capacitance values were significantly influenced by the two variables.

Table 5.4: ANOVA Response surface quadratic model for specific capacitance.

Source	Sum of Squares	df	Mean Square	F-value	P-value
Model	1.296E+05	5	25921.34	132.41	<0.0001*

A-AC	94225.60	1	94225.60	481.34	<0.0001
B-CuCo	12650.04	1	12650.04	64.62	<0.0001
AB	161.29	1	161.29	0.8239	0.3942
A^2	627.30	1	627.30	3.2	0.1166
B^2	16235.57	1	16235.57	82.94	<0.0001
Residual	1370.31	7	195.76		
Cor Total	1.310E+05	12			

R^2 = 0.9895, R^2(Adjusted) = 0.9821, R^2(Predicted) = 0.9288, *Significant

The predicted R^2 of 0.9288 is in reasonable agreement with the adjusted R^2 of 0.9821; as the difference is less than 0.2.

The findings revealed a R^2 of 0.9895. The R^2 value measures the change in the model's average value, and the value of R^2 indicates how effectively the model can predict the experimental datasets. The model is highly relevant as a result. The R^2 (predicted) was 0.9288, with a difference of < 0.2 between it and the R^2 value. It was observed that the specific capacitance values from the three electrode CV curves fitted the model's anticipated value quite well.

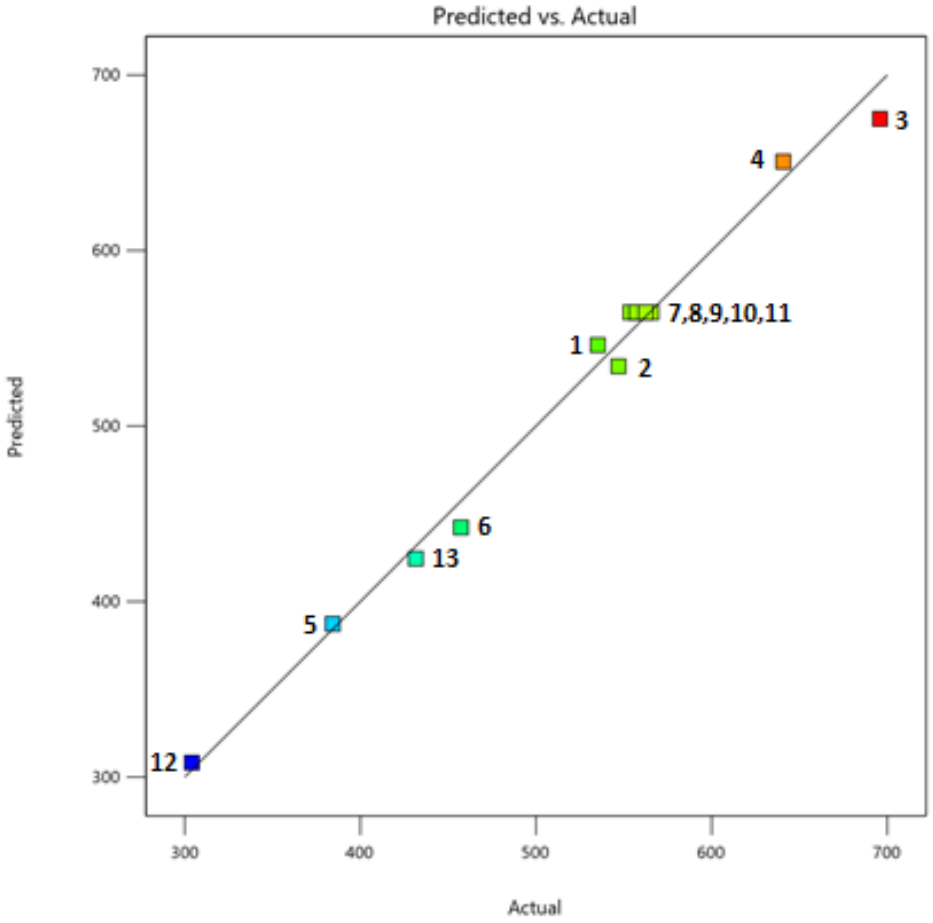
Predicted vs. Actual
Predicted
Actual
700
600
500
400
300
300
400
500
600
700
3
4
7,8,9,10,11
1
2
6
13
5
12

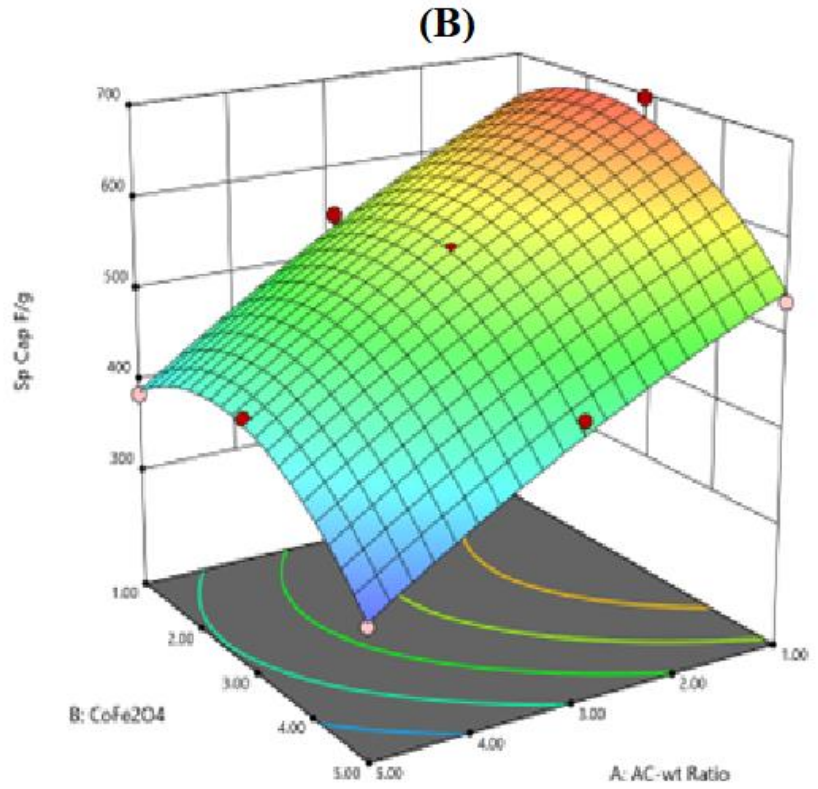
(B)
Sp Cap F/g
700
600
500
400
300
1.00
2.00
3.00
4.00
5.00
B: CoFe2O4
A: AC-wt Ratio

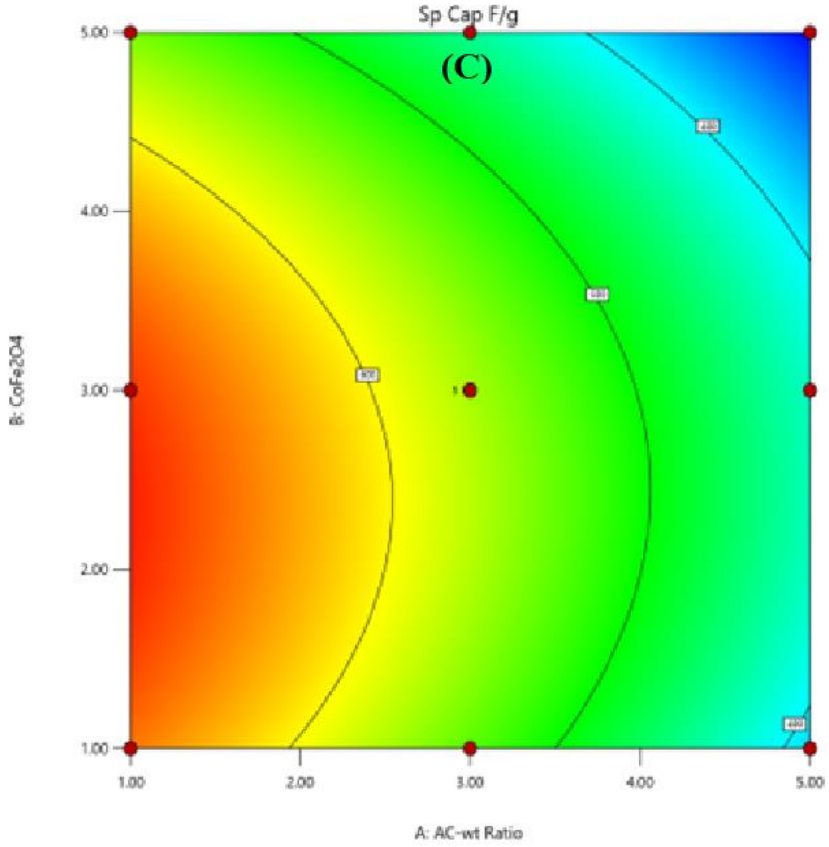
Sp Cap F/g
(C)
5.00
4.00
3.00
2.00
1.00
B: CoFe2O4
A: AC-wt Ratio

Fig. 5.13: (A) Predicted vs. actual response showing run numbers, (B) 3D response surface curve, and (C) contour plot for AC (weight percentage) vs. CoF (weight percentage) as a function of specific capacitance

The primary function and relationship of independent variables can both be studied using the 3D (three-dimensional) response surface map. In order to further analyze the connection and optimum concentrations of the two components in raising specific capacitance, RSM was utilized. The predicted vs. actual response, 3D response surface curve, and contour plot have been displayed in figure. 5.13 (A), (B), and (C), respectively. The findings demonstrate that each variable has a maximum value and that the optimization criteria are consistent and obvious. According to the analysis of the response surface method, when the weight ratio of polyaniline, activated carbon, and cobalt ferrite in the ternary composite is in the ratio of 4:1.03:2.66 (PANI/AC/CoF), the maximum value of specific capacitance is 680.1 F/g. In summary, three parallel experiments were conducted to verify the model's reliability. The specific capacitance values of 682.7 F/g, 684.2 F/g, and 687.9 F/g were obtained with a mean value of 684.9 F/g, which is consistent with the predicted value of specific capacitance, confirming that the proposed relationship model is highly accurate and reliable.

5.6.2 X-ray diffraction

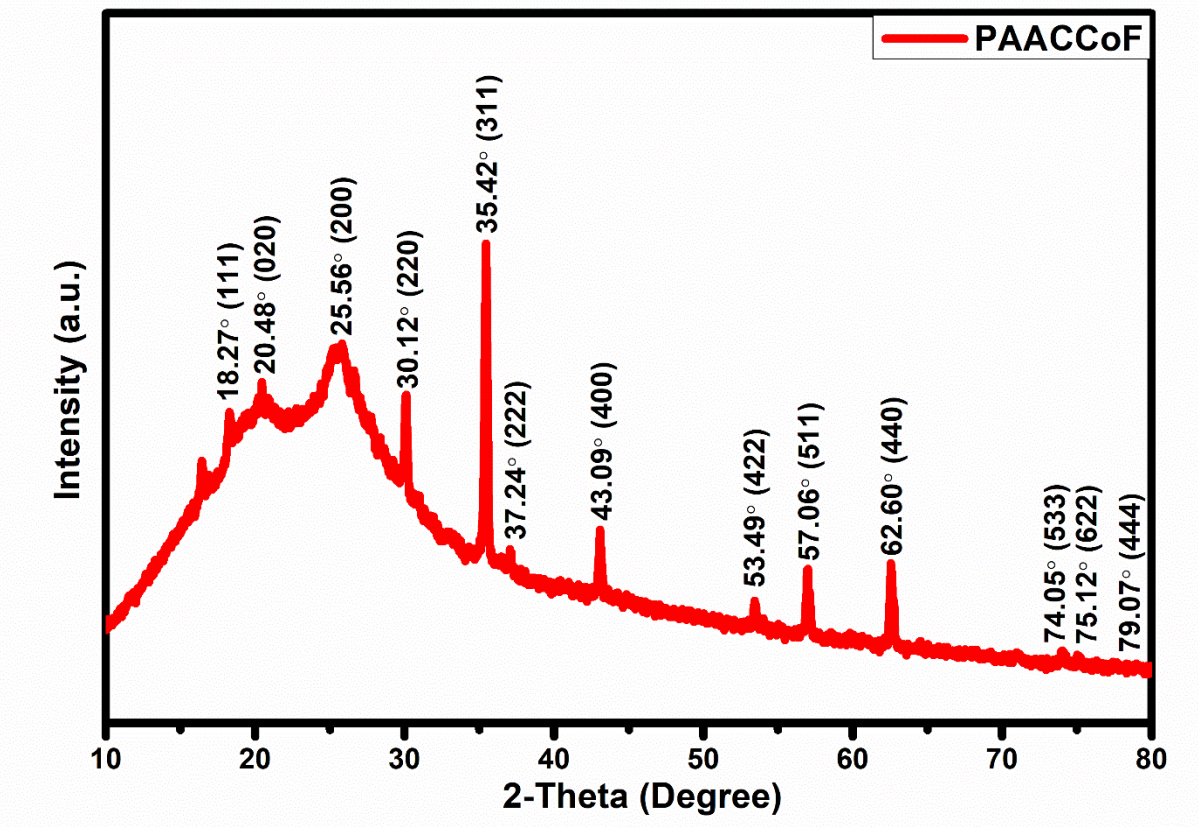

Fig. 5.14: (A) XRD patterns for the optimized ternary composite PANI/AC/CoF

The XRD pattern of the optimized ternary composite material PANI/AC/CoF has been presented in figure. 5.14. The characteristic diffraction peaks at 20.48° (020) and 25.56° (200) confirm the presence of polyaniline. The characteristic peak of AC could have been merged with the later peak of PANI and, therefore, not visible individually. The peaks at 18.27° (111), 30.12° (220), 35.42° (311), 37.24° (222), 43.09° (400), 53.49° (422), 57.06° (511), 62.60° (440), 74.05° (533), 75.12° (622), and 79.07° (444) indicate the presence of cobalt ferrite in the optimized ternary composite material PANI/AC/CoF.

5.6.3 FTIR

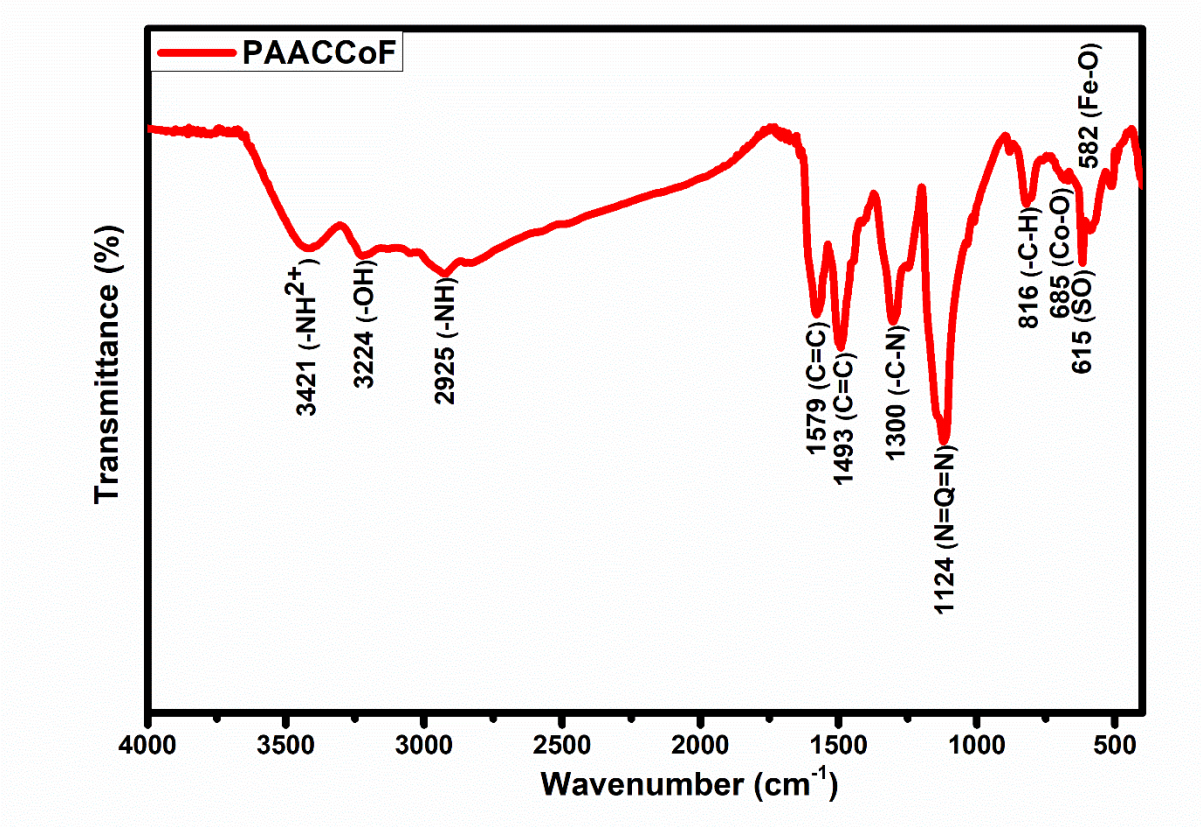

Fig. 5.15: FTIR spectra for the optimized ternary composite PANI/AC/CoF

The FTIR patterns of the optimized ternary composite material PANI/AC/CoF has been presented in figure. 5.15. The absorption bands at 3421 cm^{-1} and 3224 cm^{-1} wavenumbers correspond to $-NH^{2+}$ and -OH stretching vibrations. The band at 2925 cm^{-1} was attributed to -NH bending. Further, the vibrations at 1579 cm^{-1} and 1493 cm^{-1} were present due to C=C stretching vibrations in the quinoid and benzoid rings, respectively. Again, in the optimized ternary composite, the greater amount of benzoid form of PANI is indicated by its more intense peak. The -CN shuddering vibrations in the quinoid rings was associated with the absorption band at 1300 cm^{-1}. The p-substituted N=Q=N vibrations were referred to the peak at 1124 $cm^{-1,}$ and -CH deformations due to the presence of PTSA in PANI were attributed to 816 cm^{-1} wavenumber. The $-SO_3$ stretching due to the presence of PANI was marked at 615 cm^{-1}. Further, the absorption bands at 685 cm^{-1} and 582 cm^{-1} were present due to CoO and FeO functional groups in the optimized ternary composite material.

5.6.4 Morphological analysis

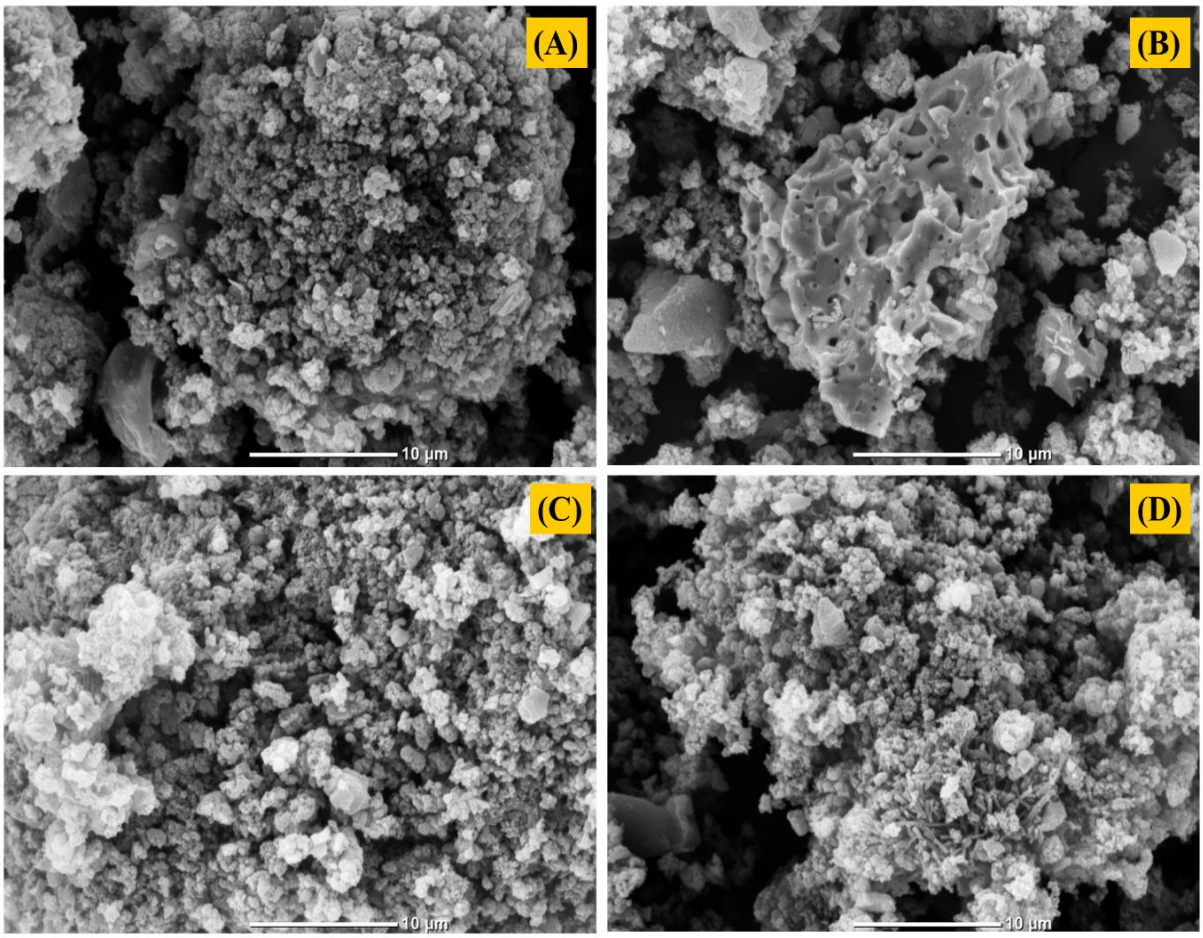

Fig. 5.16: SEM micrographs for the optimized ternary composite PANI/AC/CoF

The SEM micrographs of the optimized ternary composite PANI/AC/CoF has been provided in figure. 5.16. Micelle-like interconnected textures could be observed in the SEM images as described earlier. The large particle visible in figure. 5.16 (B) is the porous activated carbon. In the other regions, it could be seen that the polyaniline may have covered the activated carbon and cobalt ferrite particles. Rod-like structure is clearly visible in figure. 5.16 (D) as expected.

5.6.5 EDX and Elemental Mapping

The EDX spectrum of the optimized ternary composite PANI/AC/CoF has been provided in Fig. 5.17. The spectrum clearly shows the presence of all the expected elements. The elemental

mapping of the ternary composite material has been given in figure. 5.18 (combined and individual), indicating the uniform presence of all the expected elements.

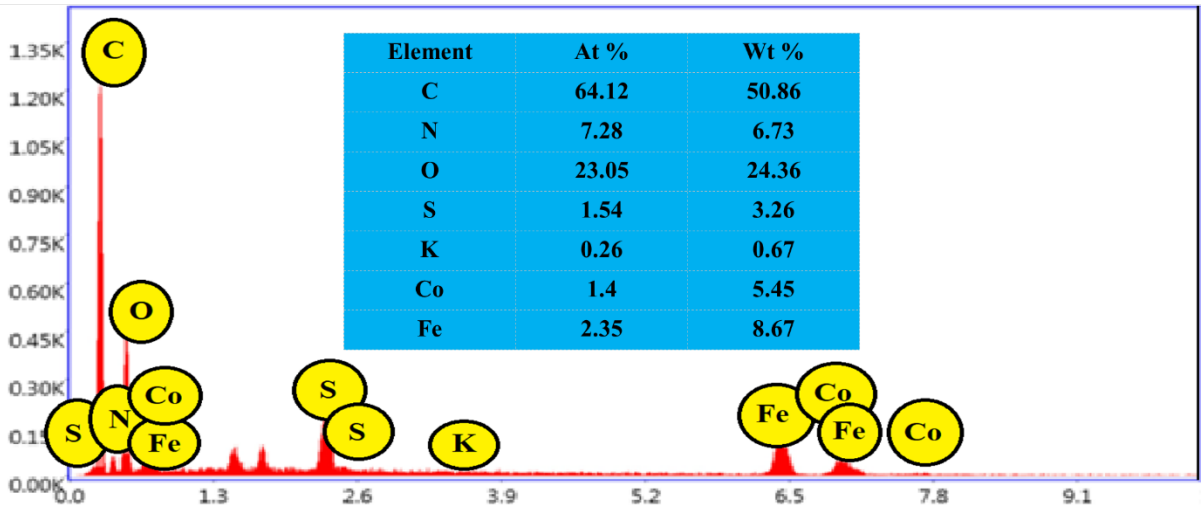

Fig. 5.17: EDX spectra of the optimized ternary composite PANI/AC/CoF

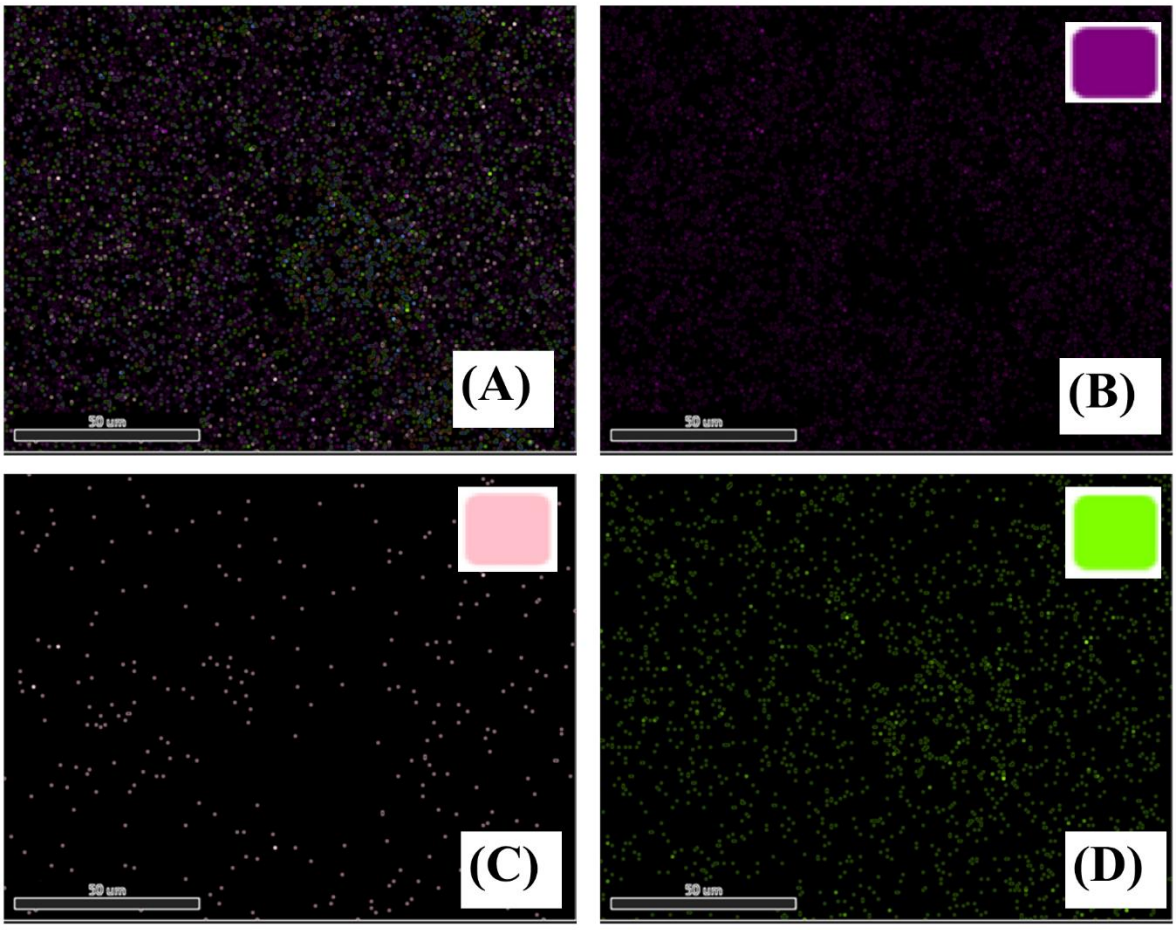

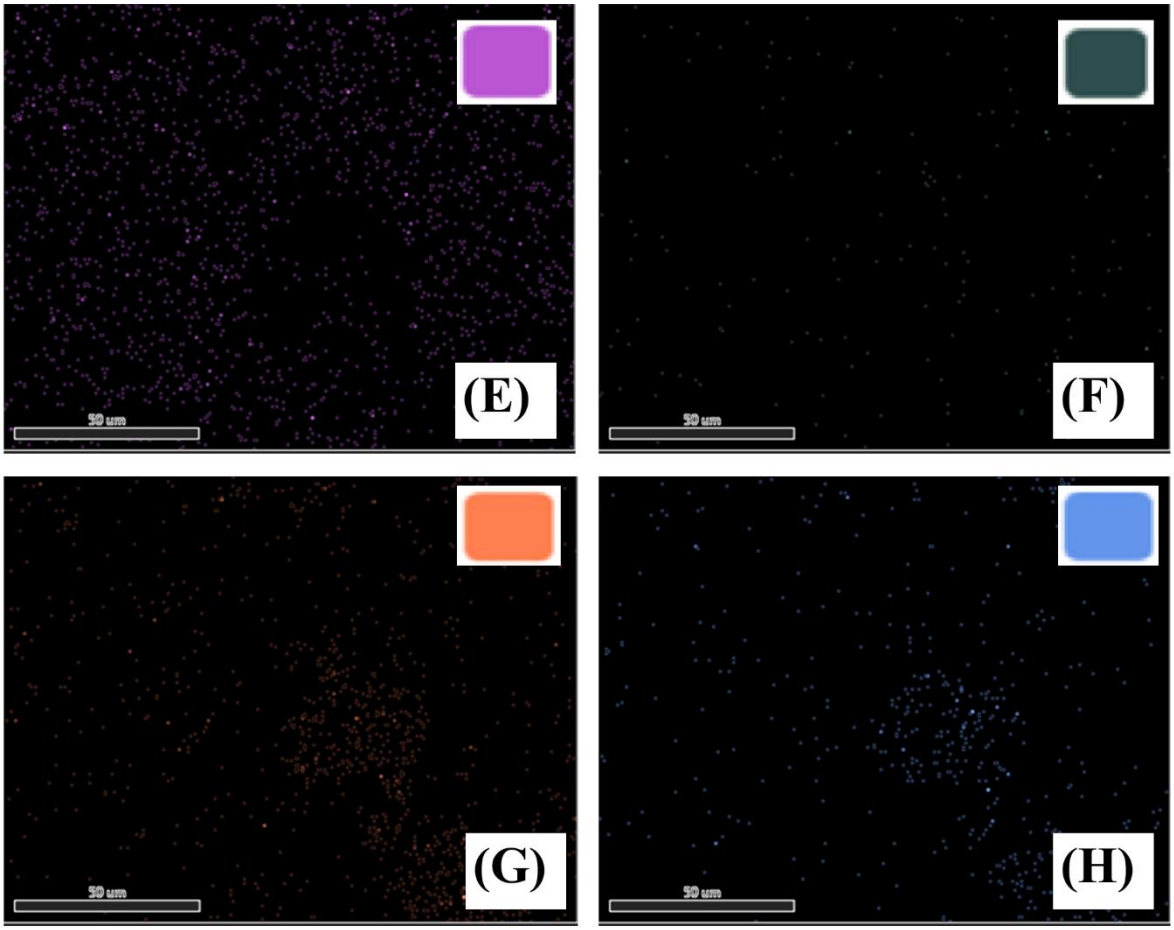

Fig. 5.18: Elemental mapping for the optimized ternary composite PANI/AC/CoF Elemental mapping for the optimized ternary composite PANI/AC/CuCo, showing (A) overlay, (B) carbon, (C) nitrogen, (D) oxygen, (E) sulfur, (F) potassium, (G) iron Fe, (H) cobalt Co.

5.6.6 Electrochemical characterizations:

Cyclic voltammetry of the prepared electrode from optimized ternary composite PANI/AC/CoF was performed in 3-E and 2-E configurations, and has been presented in figure. 5.19.

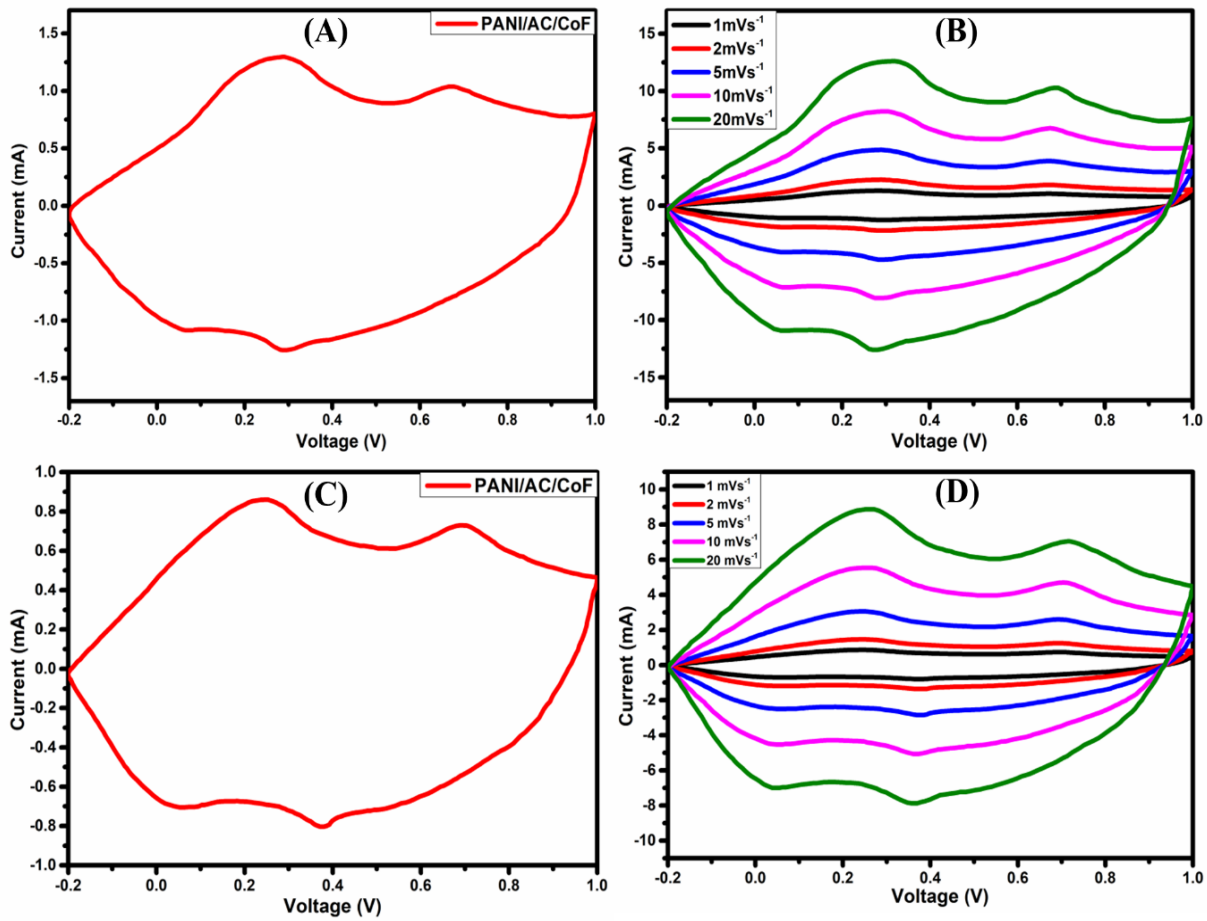

Fig 5.19: (A) 3E CV (B) 3E CV at varying scan rates, (C) 2E CV (D) 2E CV of ternary at varying scan rates for the optimized ternary composite PANI/AC/CoF

Figure. 5.19 (A) demonstrates the 3-E cyclic voltammogram where peaks in the forward scan were located at 0.26/ 0.64 V, whereas those in the reverse scan were at 0.29/0.07 V, respectively. The specific capacitance values for PANI/AC/CoF at 1 mVs^{-1} was 687.9 Fg^{-1}. The ternary composite was also tested under varying voltammetric scan rates of 2, 5, 10, and 20 mVs^{-1} (Figure. 5.19 (B)). The specific capacitance values for ternary PANI/AC/CoF at these scan rates were calculated as 596.1, 511.4, 439.8, and 337.5 Fg^{-1}. The voltammetric area under the successive curves increases with the scan rate [245], indicating the highly capacitive nature of the optimized ternary material PANI/AC/CoF. The shifting of the forward scan peaks to the right and that of the reverse scan peaks to the left side indicates strong faradaic and capacitive currents.

The prepared electrodes were also evaluated under two-electrode symmetric configuration at 1 mVs^{-1} scan rate (Figure. 5.19 (C)). The optimized ternary composite PANI/AC/CoF again demonstrated the highest voltammetric area and highest value of peak current. Further, the voltammetric area under the curves increases with the rise in scan rates to 2, 5, 10, and 20 mVs^{-1} (Figure. 5.19 (D)).

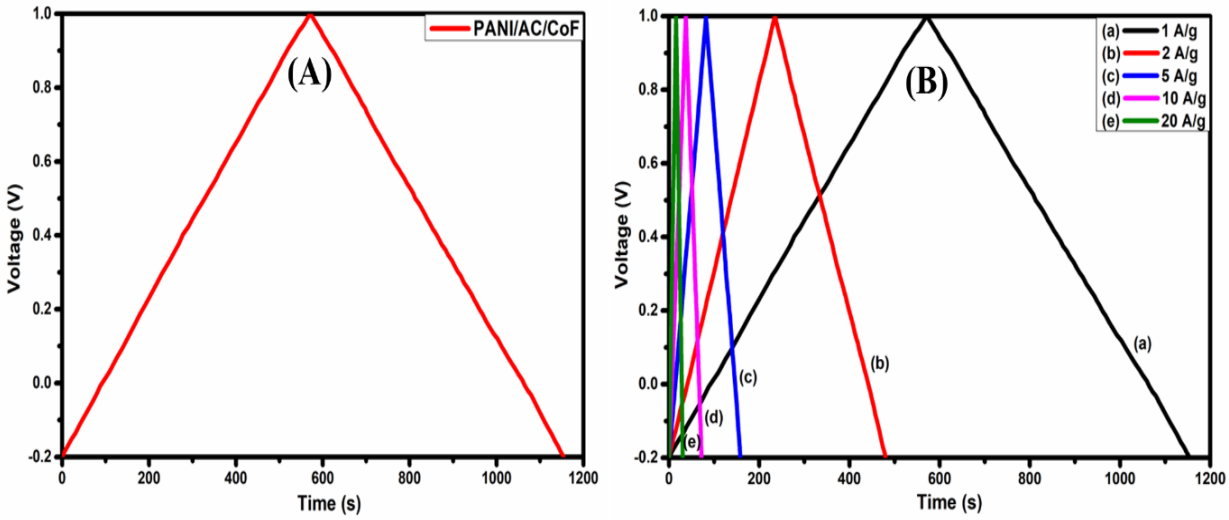

Fig 5.20: (A) 2E galvanostatic charge-discharge (B) 2E galvanostatic charge-discharge at varying current density for the optimized ternary composite PANI/AC/CoF

The galvanostatic charge-discharge tests were conducted for the optimized composite material-based electrodes under 2-E symmetric configuration. The charge-discharge plot at 1 Ag^{-1} current density is shown in figure. 5.20 (A), for which the specific capacitance was found to be 233.1 Fg^{-1}. The material demonstrated a similar triangular behavior on the charge-discharge curve with minor plateaus which are attributed to the dual behavior (EDLC and pseudocapacitive). The optimized ternary composite PANI/AC/CoF was also evaluated under varying current densities of 2, 5, 10, and 20 $Ag^{-1,}$ as shown in Fig. 5.20 (B). With the rise in current density values, a sharp decline in the charging-discharging times was observed, which is responsible for lower energy density values.

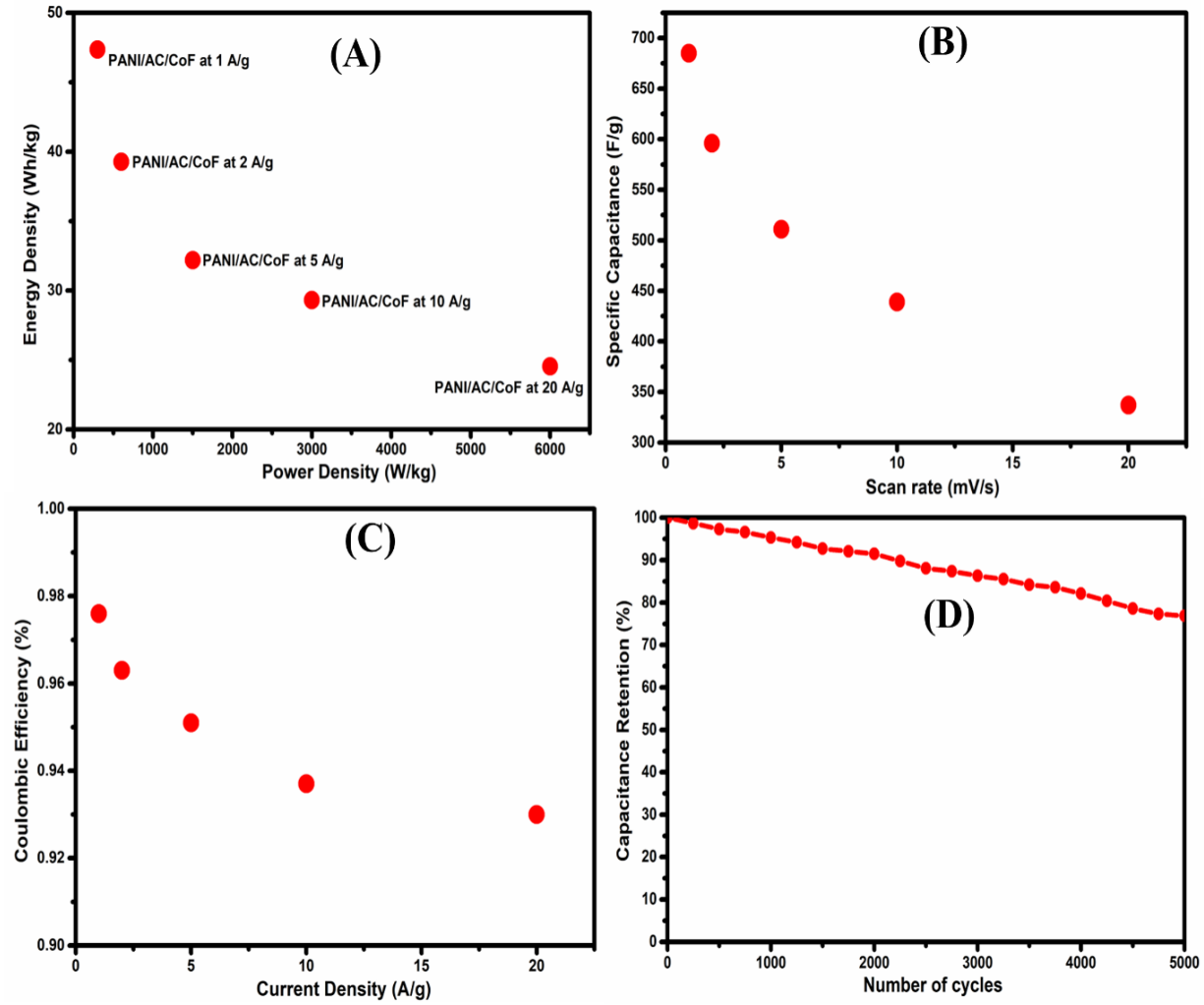

Fig 5.21. (A) Ragone plot, (B) 3E specific capacitance values at different values of voltammetric scan rates, (c) current density vs. coulombic efficiency, (D) Capacitance retention curve for the optimized ternary composite PANI/AC/CoF

Figure. 5.21 (A) shows the Ragone plot for the optimized ternary composite PANI/AC/CoF. It was observed that at higher values of current density, the specific energy density declined, whereas the specific power density increased. The peak specific energy density for the optimized ternary composite PANI/AC/CoF was 47.5 $Whkg^{-1}$ with 301.01 Wkg^{-1} of specific power density. The same ternary composite demonstrated the highest specific power density of 6000.3 W kg^{-1} with a specific energy density of 24.5 $Whkg^{-1}$ at 20 A/g. These high values of specific energy-density and specific power density correspond to the presence of both EDLC

and pseudocapacitive materials in composite material. Figure. 5.21 (B) demonstrates the variation of measured values of 3- E specific capacitance with scan rate. Figure. 5.21 (C) shows the variation of coulombic efficiency with current density, which decreases as current density increases. The capacitance retention tests for the 2E symmetric system were conducted to study the capacitance retention of the fabricated electrodes at a scan rate of 100 mV/s for 5000 cycles. The optimized ternary composite material PANI/AC/CoF exhibited outstanding capacitance retention of 76.1 % of the initial value (Figure. 5.21 (D)). Table 5.5 shows the different values of specific capacitance, specific energy-density, and specific power-density for the optimized ternary material PANI/AC/CoF.

Table 5.5: The values of specific capacitance (C_{SP}), specific energy-density (E_{SP}), and specific power-density (P_{SP}) for various prepared samples.

Material	**Scan Rate (mV/s)**	**C_{SP} (CV 3-E)**	**Current Density (A/g)**	**Esp (Wh/kg)**	**Psp (W/kg)**
PANI/AC/CoF	1	687.9	1	47.5	300.0
PANI/AC/CoF	2	596.1	2	39.2	599.4
PANI/AC/CoF	5	511.4	5	32.1	1501.1
PANI/AC/CoF	10	439.8	10	29.3	3003.2
PANI/AC/CoF	20	337.5	20	24.5	6000.3

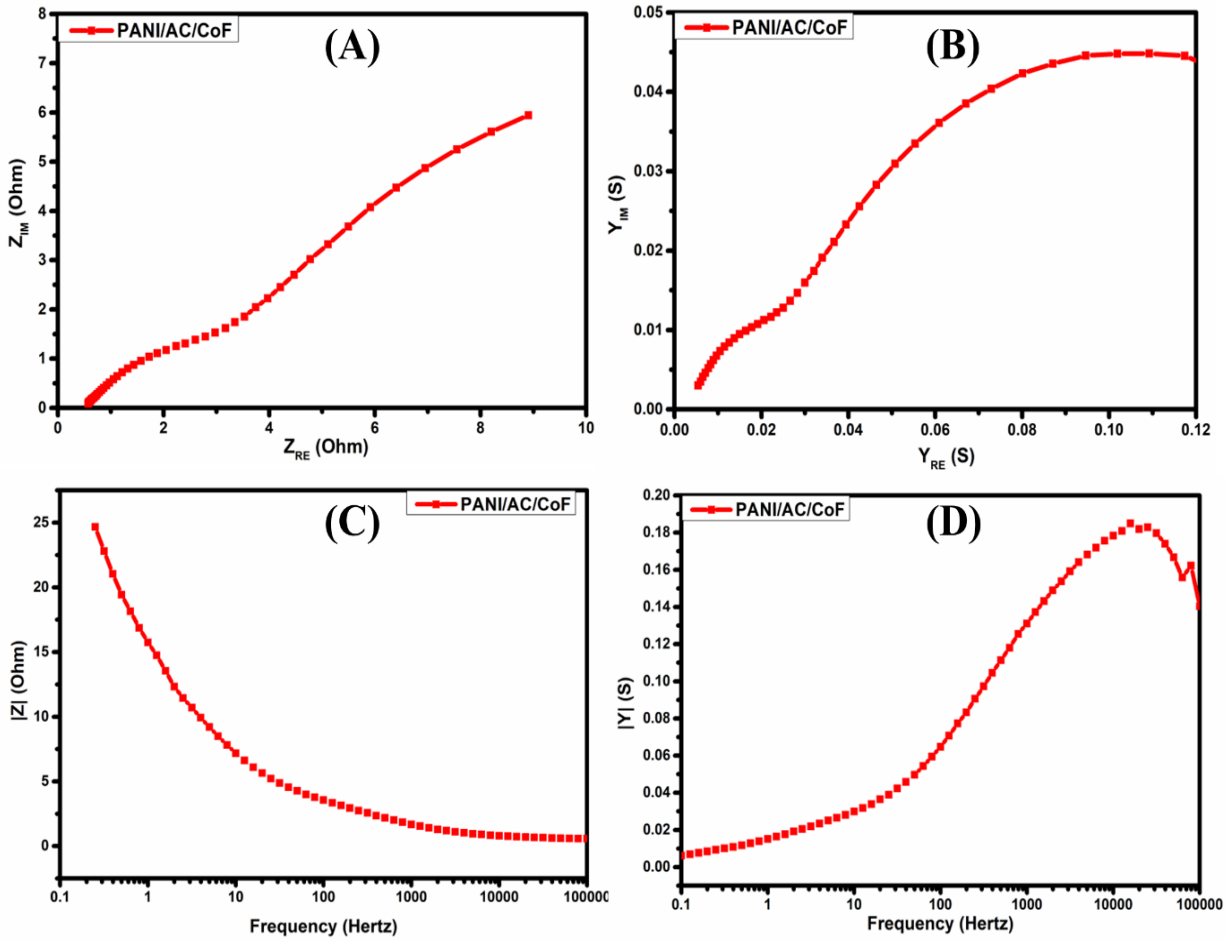

Fig 5.22: (A) Electrochemical impedance spectra (EIS) in the complex plane (B) Admittance plots in the complex plane. (C) normalized impedance |Z| vs. frequency, (D) normalized admittance |Y| vs. frequency for the optimized ternary composite PANI/AC/CoF

The impedance characteristics were also studied for the electrodes fabricated from optimized PANI/AC/CoF, and these tests were conducted in the frequency range of 0.1 to 100000 Hz. The values of ESR (equivalent series resistance) and Rct (charge transfer resistance) were calculated as 0.74 Ω and 3.26 Ω, respectively, as shown in figure. 5.22 (A). Further, the admittance properties of the fabricated electrodes were also studied in the form of Y_{RE} vs. Y_{IM} plots. Figure. 5.22 (B) shows the variation of real admittance (Y_{RE}) vs. the imaginary admittance (Y_{IM}) for the fabricated electrode from optimized PANI/AC/CoF. Figure 5.22 (C) shows the variation impedance |Z| with frequency. It was noticed that |Z| decreases with a rise

in frequency. Figure 5.22 (D) shows the variation of |Y| vs. frequency. It was observed that with the rise in frequency, |Y| increases as electrolyte ions vibrate faster at higher frequencies as opposed to |Z|.

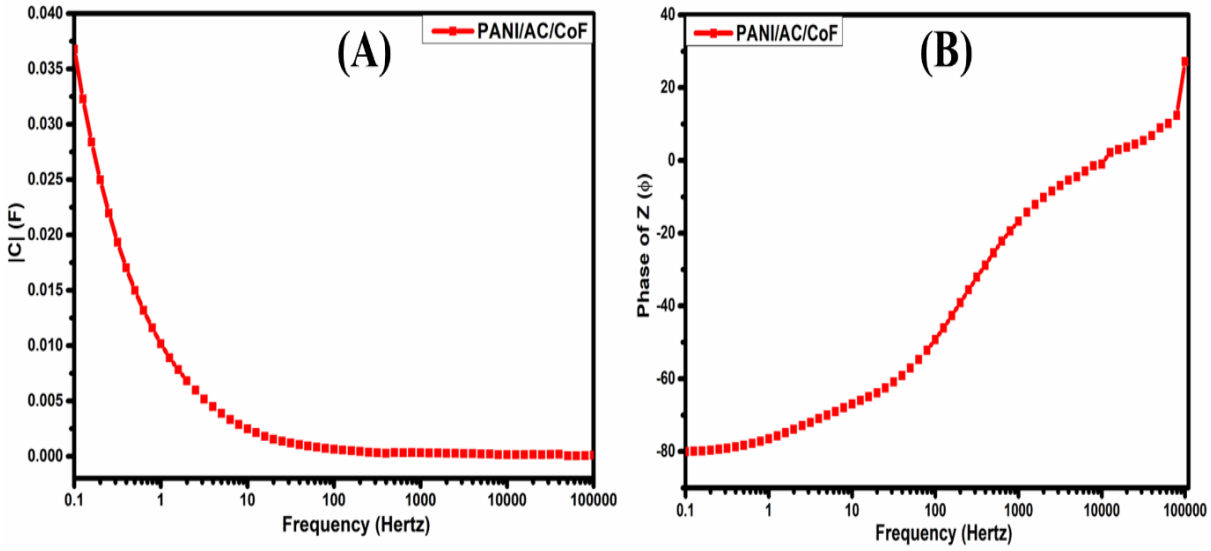

Fig 5.23: (A) normalized capacitance |C| vs. frequency, and (B) phase of |Z| (ϕ) vs. frequency of the optimized ternary composite PANI/AC/CoF

Figure. 5.23 (A) manifests the change of capacitance |C| with frequency. The value of total or normalized capacitance decreases with a rise in frequency, which agrees with the EIS results. Figure. 5.23 (B) shows the variation of the phase of Z (ϕ) with frequency for the optimized PANI/AC/CoF. The phase angle in the low-frequency regime is about 80°, indicating its highly pseudocapacitive nature.

5.7 Conclusion:

In the current research, the composite material based on polyaniline, activated carbon, and cobalt ferrite (PANI/AC/CoF) has been optimized based on varying weight ratios of AC and CoF with the help of Response Surface Methodology (RSM). The composite material with the proportion of 4:1.03:2.66 polyaniline, activated carbon, and cobalt ferrite shows excellent specific capacitance of 687.9 F/g in three-electrode configuration. The optimized ternary

composite material demonstrated the highest specific energy density of 47.5 Wh/kg and specific power of 6000.3 W/kg. It offers a high capacitance retention of 76.1 % after the completion of 5000 cycles. The charge transfer resistance of the optimized ternary composite material PANI/AC/CoF was 3.26 Ω. Based on the above discussions, it can be concluded that on the basis of specific capacitance values, the optimized ternary composite material with a weight ratio of 4:1.03:2.66 (PANI: AC: CoF) was found to be the best material.